

Drag variations, tidal asymmetry and tidal range changes in a mangrove creek system

Erik M. Horstman^{1,2} | Karin R. Bryan^{2,3} | Julia C. Mularney²

¹Water Engineering & Management, Faculty of Engineering Technology, University of Twente, PO box 217, Enschede, AE, 7500, the Netherlands

²Coastal Marine Group, School of Science, University of Waikato, Private Bag 3105, Hamilton, 3240, New Zealand

³Environmental Research Institute, University of Waikato, Private Bag 3105, Hamilton, 3240, New Zealand

Correspondence

Erik M. Horstman, Water Engineering & Management, Faculty of Engineering Technology, University of Twente, PO box 217, 7500 AE, Enschede, the Netherlands.
 Email: e.m.horstman@utwente.nl

Funding information

Marsden Fund; Royal Society of New Zealand

Abstract

Aboveground root structures enhance drag on tidal currents in intertidal mangrove forests, whereas the creeks dissecting such forests provide low-resistance conduits for tidal flows. Here, observations from an established mangrove forest in the Whitianga Estuary, Aotearoa New Zealand, are used to investigate the variability of the drag experienced by tidal flows in a mangrove creek system and subsequent effects on tidal asymmetries and ranges.

Tidal flow speed maxima in the creek occurred at overbank water levels during the sheet flow stage on rising tides, but at water levels below the creek bank (the creek flow stage) on falling tides. Inferred bulk drag coefficients for the creek were greater during the sheet flow than the creek flow stage, and were linearly correlated with the bulk drag coefficients at stations in the adjacent forest. Although falling tides, associated with larger bulk drag coefficients, had an increasingly longer duration than rising tides towards the back of the forest, we observed ebb-dominant flow speed asymmetry that declined inland in the creek. Conversely, flow speeds within the forest were consistently flood-dominant, in accordance with smaller bulk drag coefficients during rising tides. Along the full length of the mangrove system, high-water levels were lowered by up to 12 cm/km within the creek and 36 cm/km within the mangrove forest.

Creek bed roughness associated with bulk drag coefficients observed in deeper parts of the creek was much greater than the hydraulic roughness of the sediment. For accurate simulations of landscape-scale feedbacks between the creek and mangrove forest, incorporating both direct and indirect contributions of the vegetated forest platform to creek bed roughness is essential. These findings show that the interaction between creek flow and sheet flow in a mangrove creek system is a key driver of tidal asymmetries as well as the attenuation of high-water conditions.

KEY WORDS

mangroves, Avicennia marina, dissipation, drag coefficients, tidal dynamics, creek flow

1 | INTRODUCTION

The functioning and survival of intertidal mangrove ecosystems are governed by interactions between vegetation, flows and landforms. Hydrodynamic conductivity and ecological development are strongly coupled in these intertidal systems: tidal and riverine water provides a

vital supply of nutrients and sediments to the mangroves, whereas more dense vegetation and higher bed level elevation reduce connectivity between intertidal areas and creeks (Lara et al., 2009; Larsen, 2019; Perillo, 2019). This balance is both a prerequisite for, and an inherent consequence of, the capacity of mangroves for ‘ecosystem engineering’ (Jones et al., 1994, 1997). Mangroves’

This is an open access article under the terms of the Creative Commons Attribution-NonCommercial-NoDerivs License, which permits use and distribution in any medium, provided the original work is properly cited, the use is non-commercial and no modifications or adaptations are made.
 © 2021 The Authors. *Earth Surface Processes and Landforms* published by John Wiley & Sons Ltd.

aboveground root structures, stems and the lower parts of the canopies provide substantial drag to tidal currents propagating through intertidal forests, reducing both tidal speed and amplitude (Horstman et al., 2015; Mazda et al., 2005; McIvor et al., 2012; Montgomery et al., 2019) while enhancing sediment deposition rates (Adame et al., 2010; Bryan et al., 2017; McIvor et al., 2013; Van Santen et al., 2007; Wolanski, 1995). The inundation regime of these forests controls the degree to which resources (sediments as well as nutrients) are delivered and stresses due to tidal currents and waves (regulators) are distributed, inducing environmental gradients that control the biogeomorphologic development of the mangrove forest (Alongi, 2009; Bryan et al., 2017; Twilley & Rivera-Monroy, 2009; Twilley et al., 1999). Consequently, there exists a negative feedback between the supply of resources, enhanced sediment deposition and vegetation development, and the inundation frequency of the forest, which results in distinct zonation and succession patterns in mangroves (Bryan et al., 2017; Horstman et al., 2018b; Van Loon et al., 2007; Watson, 1928).

Creeks provide low-resistance conduits through vegetated intertidal areas, funnelling tidal currents through unvegetated channels with greater water depths (Bayliss-Smith et al., 1979; Friedrichs, 2010). While improving the transport of suspended and dissolved matter (resources) into intertidal areas (Allen, 2000; Christiansen et al., 2000; Fagherazzi et al., 2013), creeks may substantially reduce the attenuation of long waves in mangrove systems (Krauss et al., 2009; Montgomery et al., 2018; Zhang et al., 2012), thus reducing the ability of mangrove systems to serve as coastal ecosystem defences. Despite the key role of creeks in the functioning of vegetated intertidal areas, the properties of these tidal networks lack the generic scaling relations that are found in fluvial systems (Rinaldo et al., 1999a), where channelisation scales with, for example, catchment area and slope (Montgomery & Dietrich, 1992). Rinaldo et al. (1999a) attribute the absence of such scale-invariant tendencies to complex bi-directional tidal dynamics shaping these tidal networks and spatial heterogeneity in vegetation and sediment properties, as well as pre-existing features from previous stages of the biogeomorphologic development of the creek network.

Two distinct flow regimes occur during tidal flooding and drying of creek-incised intertidal areas. These regimes are separated by a biogeomorphologic threshold formed by the bank elevation of the creek combined with the height of the (densest) vegetation on the intertidal platform (Horstman et al., 2013; Temmerman et al., 2005). The *creek flow stage* occurs at water levels below this threshold, during which tidal flows are confined within (and closely adjacent to) the creek, and the *sheet flow stage* occurs for overbank water levels exceeding the threshold, when tidal exchange between the platform and open water occurs directly above and across the seaward vegetation fringe. When tidal water levels exceed this biogeomorphologic threshold, rotation of the flow on the platform occurs with creek-normal flows during the creek flow stage, transitioning to predominantly creek-parallel flows during the sheet flow stage (Horstman et al., 2013; Temmerman et al., 2005). Differences in the hydraulic resistance between the deep unvegetated creeks and shallow vegetated intertidal platforms allow for flow speeds within the creek that are an order of magnitude greater [$O(10 \text{ cm/s})$] than those on the platform [$O(1 \text{ cm/s})$] (Horstman et al., 2013; Wolanski, 1992). Consequently, for the creek flow regime, water entering the vegetated platform at rising tide

(or exiting during falling tide) is slowed down, inducing a negative (positive during ebb) water level gradient away from the creek and an ebb-dominant tidal asymmetry of the flow speeds in the creek (Mazda et al., 1995). During the sheet flow regime, when the tidal wave propagates over the vegetated platform, fringe-normal (i.e. creek-parallel) water level gradients are observed between the platform and the open water (as would be observed similarly across a contiguous platform that is not incised by creeks (Montgomery et al., 2018). These tidally induced water level gradients are the main driver for landscape-scale surface flows in friction-dominated vegetated intertidal areas (Friedrichs & Madsen, 1992; Mularney & Henderson, 2018).

This work focusses on the landscape-scale feedbacks between the creek and the surrounding mangrove forest through observations of the interactions between the creek flows and sheet flows in a mangrove system. Concurrent observations in creeks and on the vegetated platforms unveiling such interactions of creek and sheet flows in mangroves are lacking. Initially, mechanical flow meters were too large to monitor flow velocities within the dense mangrove vegetation (Wolanski et al., 1980). Since the development of much smaller acoustic current meters, changing flow patterns have been monitored along transects across creeks and mangrove forest fringes (Horstman et al., 2013; Mularney et al., 2017a; Willemse et al., 2016). These field studies have insufficient spatial coverage and resolution for direct observations of the interactions between creek and sheet flows, compared with similar studies in salt marsh environments (Stark et al., 2015; Vandenbruwaene et al., 2015; Young et al., 2016). At the same time, resolving relatively small water level gradients in vegetated intertidal areas (the main driver of surface flows in high-friction areas) from concurrently deployed pressure gauges remains challenging because of inaccuracies in bed level measurements and the inability to level instruments with a ‘horizontal water level-assumption’ across a vast mangrove system as the water level gradient never fully disappears (Allen, 2000; Horstman et al., 2013; Young et al., 2016).

To date, most insights on the landscape-scale flow patterns in intertidal mangroves (and salt marshes) have been obtained from numerical studies of vegetation–flow–landform interactions (Aucan & Ridd, 2000; Horstman et al., 2015; Mazda et al., 1995; Temmerman et al., 2005; Wolanski et al., 1980). These numerical models critically depend on the parameterisation of the vegetation-induced drag. The first modelling attempts represented vegetation-induced drag on the forest platform by an increased uniform bed roughness (Aucan & Ridd, 2000; Mazda et al., 1995; Wolanski et al., 1980). Recent advances in process-based numerical modelling have allowed vegetation-induced drag and turbulence to be taken into account, representing the vegetation by (multiple layers of) rigid vertical cylinders with explicit (spatially varying) diameters and densities (Horstman et al., 2015; Temmerman et al., 2005). These approaches are supported by numerous flume studies indicating the different flow profiles and impacts on bed shear stresses, in vegetated flows compared with flat bottoms with an increased bed roughness (reviewed in e.g. Mularney & Henderson, 2018; Nepf, 2012; Tinoco et al., 2020). Following these experimental results, analytical solutions have also been provided for improved parameterisations of the representative vegetation roughness (Baptist et al., 2007). Quantification of momentum losses, either computed directly from the vegetation drag or indirectly with a representative vegetation roughness, deploy a spatially

averaged vegetation density and often assume an element drag coefficient C_d [–] equal to 1 (Baptist et al., 2007; Horstman et al., 2015; Temmerman et al., 2005). However, flume experiments have shown the dependency of the element drag coefficient on the vegetation density and its various geometrical properties (Horstman et al., 2018a; Nepf, 1999; Tinoco et al., 2020). These effects have not yet been incorporated into vegetation parameterisations in numerical models because of limited data availability from laboratory and field studies to test and validate such models (Larsen, 2019; Tinoco et al., 2020).

In this study, we investigate the relationship between the creek and the surrounding intertidal mangrove forest platform and its role on controlling the flow speeds and directions, as well as the tidal propagation. We hypothesise that the sheet flow over the vegetated platform affects flow speeds and tidal asymmetry within the creek and, vice versa, that the creek flow affects the flow speed and tidal attenuation across the vegetated platform. Insufficient resolution (e.g. in Bryan et al., 2017), site complexities (e.g. in Horstman et al., 2013) and instrument limitations (e.g. in Wolanski et al., 1980) have made it difficult to isolate the role of this connection in previous studies (Larsen, 2019). Here, we show new measurements from a relatively simple tidal mangrove creek system with no direct freshwater input. We present synoptic data of water levels and flows along the full length of the creek and on the adjacent vegetated platform, as well as comprehensive morphological and vegetation data. The extent of the system (almost 1 km length) allowed for resolution of along-creek water level differences that exceeded inaccuracies in the bed level elevation data. Specifically, we use these comprehensive landscape-scale data to explore: (1) tidal attenuation in the creek dissecting the mangrove platform and induced tidal asymmetries in both the creek as well as on the vegetated platform; (2) the drag forces in the creek and on the vegetated mangrove platform and explore how the relative forces control the evolution of tidal asymmetry; (3) the effect of vegetation and platform characteristics on the creek flow dynamics; and (4) to what extent the sheet flow dynamics on the mangrove platform depend on the presence of a creek.

2 | METHODS

2.1 | Study site

The Whitianga Estuary, on the North Island of New Zealand (Figure 1a), is about 6 km long and up to 4 km wide, with a total area of 12.9 km² (Jones, 2008). Well-established mangroves (*Avicennia marina* var. *australisica*) and salt marsh vegetation dominate the inner (southern) half of the estuary where they cover extensive intertidal flats (Reeve, 2008). Mangrove trees in the Whitianga Estuary reach heights of 6–8 m and stem diameters of up to approximately 20 cm (Graeme, 2009; Horstman et al., 2018b), even though climatic stresses near the global southern limit of mangrove extent at 38° S generally constrain mangrove growth (Duke et al., 1998; Spalding et al., 2010; Tomlinson, 1986).

At the upper end of one of the arms in the central part of the Whitianga Estuary (36°52'56"S, 175°42'2"E), an ~800-m-wide mangrove complex is dissected by a number of well-defined creeks (Figure 1a,b). The study site comprises a single creek and its surrounding ‘catchment’ as demarcated in Figure 1c. The creek catchment has

no direct freshwater input from the land and, apart from intermittent rainfall, flow patterns in this area are purely tide-driven. In higher parts of the study site and at the landward extent of the intertidal areas, vegetation is predominantly composed of salt marsh species such as saltmarsh ribbonwood, sea rush and oioi (Graeme, 2009), showing up as darker-green and brownish-green shaded areas surrounding the mangroves of the creek catchment in Figure 1b. The salt marsh vegetation also encroaches on the mangroves on the raised ridges just inland of the forest fringes north and south of the creek mouth (Figure 1b,c).

Instrument stations were installed in the thalweg of the creek at intervals of 100–200 m (stations C0–C6; Figure 1c), avoiding sharp creek bends and local perturbations of the creek bed that would affect local flow profiles. Creek-normal transects were defined for each of the creek stations, and additional instruments were installed on the mangrove forest platform at distances of 10–50 m away from the creek (Figure 1c). Forest stations were positioned north of the creek (F2N–F6N) and were duplicated at two locations south of the creek (F2S, F4S).

2.1.1 | Bathymetry

A manual RTK GPS (Trimble R8 GNSS) survey was performed to collect elevation data of both the creek and vegetated platform across the study site, as well as the unvegetated mudflats at the creek entrance. Local geodetic marks (Land Information New Zealand, LINZ) were used to obtain an accurate vertical datum [$O(10^{-2})$ m accuracy]; however, tree cover and reception issues at this remote site reduced vertical survey accuracy by up to one order of magnitude. A continuous elevation map of the study site was reconstructed from a 2012 LiDAR map of the study site (Waikato Regional Council). LiDAR data showed good agreement with our survey data ($R^2 = 0.88$), for all elevations above –0.4 m + MSL, after correction for a fixed reference datum offset. The deeper parts of the creek (representing a negligible fraction of the total study site, Figure 1d) could not be reconstructed appropriately from the LiDAR map. Consequently, for the cross-sectional properties of the creek (summarised in Table 1) LiDAR data were substituted with survey data collected along the creek-normal transects indicated in Figure 1.

The catchment of the studied mangrove creek system in Figure 1c was delineated based on (i) the elevation contour of the highest high-water level; (ii) the highest elevation contour between neighbouring creek systems; and (iii) a cross-shore line (perpendicular to the elevation contours) across the forest fringe at either side of the creek mouth. The hypsometry of the catchment (Figure 1d) shows an inflection point at 0.6 m + MSL, indicating a rapid increase of the intertidal area at this elevation. The elevation threshold separating the creek from the mangrove forest platform was defined as 0.2 m + MSL, equal to the minimum elevation of the vegetated platform near the mouth of the creek (shaded white in Figure 1c). The mean elevation of the mangrove platform was 0.75 m + MSL (PLE50), with the 10th and 90th percentiles of the platform elevation (PLE10 and PLE90) only spanning 0.46 m of elevation difference (Figure 1d). Creek and platform properties were measured along each transect (Table 1). The creek width and lowest bed level of the creek (all instruments were deployed at the creek thalweg) show irregular variations,

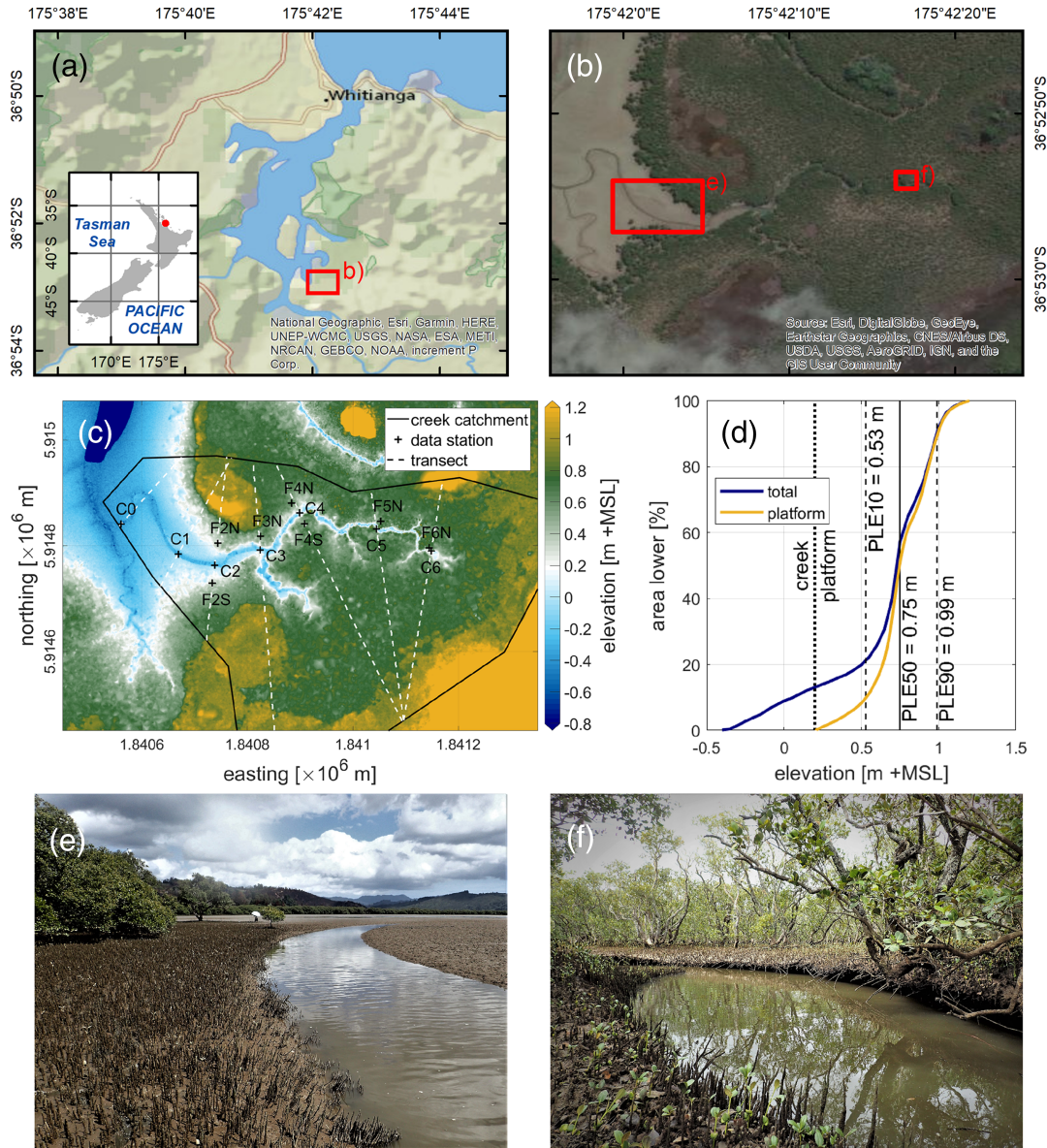


FIGURE 1 (a) Map of the Whitianga estuary (inset shows its location within New Zealand); (b) aerial photograph of the study site, boxes indicating locations of photos (e,f); (c) corrected LiDAR elevation map of study site (white = elevation threshold between creek and forest platform, green = mangrove forest, yellow = salt marsh) with instrument stations (stations are named C# for creek stations and F#N/S for forest stations north and south of the creek, respectively) and delineation of the creek catchment, including the creek-normal transects; (d) hypsometry of studied creek catchment with PLE10/50/90 indicating the 10/50/90th percentile of the mangrove platform elevation; (e) photo of the creek mouth between stations C2 and C3 (looking seaward) showing the transition from densely vegetated creek banks to an unvegetated mudflat; and (f) photo of the creek near station C5 (looking inland) showing an overhanging creek bank and vegetation (for more photos of the course of the creek we refer to Figure S1-S6 in the Supporting Information). Maps courtesy National Geographic/ESRI (a) and ESRI/DigitalGlobe (b); LiDAR data courtesy Waikato regional council (c) [Color figure can be viewed at wileyonlinelibrary.com]

with no clear inland trend. The total sub-catchment area inland of each creek-normal transect and the volume-percentage of water stored in those sub-catchments at the highest high-water level were estimated assuming no water level gradient.

2.1.2 | Vegetation

Vegetation properties were mapped throughout the forest platform, at each of the forest stations adjacent to the instrument stations within the creek (Figure 1c). Stem densities (N [m^{-2}]), heights (h_{veg} [m]) and diameters (d [m], at 30 cm above the bed) of the

trees were surveyed in of 5×5 m tree plots. Mangrove pneumatophores were counted in five quadrats of 0.5×0.5 m at fixed positions in the tree plots (at each corner and in the centre). Heights and diameters (bottom, middle and top of the pneumatophore) were collected for five pneumatophores (at each corner and in the centre) in each quadrat. For each plot, we then computed the average frontal area density a [m^{-1}] and the total solid volume fraction φ [–] of all vegetation elements combined (Table 1):

$$a = Nd; \quad (1)$$

TABLE 1 Biogeomorphological properties for each sub-catchment of the studied mangrove system, as defined in Figure 1. Along-creek distance is the inland distance from station C0 following the thalweg of the creek. Bed level, bank level, creek orientation and creek width were determined at each station C0–C6. Transect width is the total length of the creek-normal transect lines depicted in Figure 1. The (cumulative) area and volume were computed for the sub-catchments inland of the consecutive transect lines, for the highest high tide assuming no water level gradient. Vegetation properties were obtained at the platform stations adjacent to each creek station, as described in Section 2.1.2

Transect	Along-creek distance to C ₀ [m]	Bed level creek [m + MSL]	Bank level [m + MSL]	Creek orientation [[°] N]	Creek width [m]	Transect width [m]	Subcatchment area [$\times 10^4$ m ²]	Subcatchment volume[% at HHWL ^b]	Pneumatophore density [m ⁻²]	Pneumatophore height [cm]	Total mangrove densitya [m ⁻¹]	Total mangrove density [m ⁻¹]
C0	0	-0.84	-0.20	236	10	175	31.3	100	-	-	-	-
C1	233	-0.67	0.00	108	14	262	28.2	78.5	B: ^a 2	13.5	B:0.0096	B:0.0000
C2	306	-1.01	0.10	84	18	333	26.6	70.2	B: ^a 128 F: ^a 390	B:9.4 F:5.9	B:0.9327 F:3.6637	B:0.0053 F:0.0184
C3	400	-1.18	0.40	92	9	550	22.2	58.8	469	7.6	3.5622	0.0230
C4	512	-1.21	0.50	49	8	542	14.0	36.1	463	5.2	3.4556	0.0203
C5	706	-1.33	0.55	134	13	440	10.2	23.5	662	2.8	3.9812	0.0246
C6	849	-0.43	0.60	82	3	450	7.18	14.6	525	4.6	3.7696	0.0263

^aB = bank; F = forest, where there is a distinct difference between a less vegetated bank and a denser vegetated platform

^bHHWL = highest high-tide water level

$$\varphi = \frac{\pi}{4} N d^2. \quad (2)$$

At transect C1, vegetation was surveyed at the narrow and sparsely vegetated creek bank only, as the forest fringe was very narrow and quickly transitioned into the raised ridges just inland of the forest fringe (Figure 1c). However, at transect C2, separate vegetation plots were surveyed at the sparser vegetated bank of the creek and the denser vegetated forest platform (Table 1). Further inland, creek bank levels rapidly increased to the platform elevation and, consequently, vegetation properties at the creek banks resembled those on the forest platform.

2.2 | Hydrodynamic data

2.2.1 | Instruments and data collection

Field data were collected from 10 to 22 February 2017. An extensive network of acoustic flow meters and pressure gauges was deployed to obtain a synoptic dataset of the tidal creek and forest flows through the study site. The measurement network consisted of an acoustic doppler profiler (ADP; Sontek Argonaut) and six acoustic doppler current profilers (ADCP; 2 MHz Nortek Aquadopps) at stations C0–C6. On the platform, four high-resolution ADCPs (2 MHz Nortek Aquadopps operating in pulse-coherent mode) were positioned at stations F2N/S and F4N/S (Figure 1c), two acoustic doppler velocimeters (ADV; Nortek Vector) at F3N and F5N, and one ADV (Sontek Triton) at F6N.

All ADCPs and the ADP were installed on the bed, in upward-looking positions. The vector ADVs were deployed upward-looking (i.e. with the prongs facing the bed), and the Triton ADV was deployed sideways owing to instrument constraints. The ADCPs deployed in the creek measured velocity profiles through the full water depth with 10 cm vertical resolution, whereas the ADCPs in the forest captured a short profile of 45 cm with 2.5 cm vertical resolution (Table 2). Data collection settings of each instrument are summarised in Table 2, along with the height above bed of the flow monitoring volume (or the lowest cell for the profilers) and the local bed level elevation. Internal pressure sensors of all instruments were used for concurrent monitoring of the water levels throughout the area (accounting for the variable heights above bed of these pressure sensors). Fast instrument sampling rates and relatively short burst intervals (Table 2) allowed for a high-resolution data record of the creek and sheet flows throughout the mangrove creek system, as well as the water level gradients.

The atmospheric pressure at mean sea level was obtained from a 10-min meteorological record for the nearby Whitianga airport, accessed through the CliFlo database of New Zealand's National Institute of Water and Atmospheric Research (<https://cliflo.niwa.co.nz/>).

2.2.2 | Data processing

Flow data from all acoustic instruments were filtered first to remove low-quality data. Data above the water surface and signal strengths

TABLE 2 Summary of instruments deployed at the stations mapped in Figure 1c: the ADP (Sontek Argonaut), ADCPs and high-resolution (HR-)ADCPs (Nortek Aquadopp) were all deployed level on the bed, collecting flow profile data right to the water surface (number of cells and cell size listed, along with the height above bed of the instruments as well as their monitoring volumes). ADVs (Nortek vector and Sontek triton) were deployed upward and sideways looking, respectively, collecting single-point near-bed flow data (cell size and heights above bed of the instruments as well as their monitoring volumes as indicated). All instruments had built-in pressure sensors at the heights indicated

Instrument station	Instrument	Measurement cells	Cell size [mm]	Burst sampling [s]	Burst interval [s]	Flow sensor height above bed ^a [m]	Flow monitoring height above bed ^a [m]	Pressure sensor height above bed [m]	Bed level [m] + MSL]
C0	ADP	10	250	60 (@20 Hz)	90	0.23	0.55	0.23	-0.84
C1	ADCP	25	100	60 (@23 Hz)	90	0.12	0.32	0.08	-0.67
C2						0.12	0.32	0.08	-1.01
C3						0.11	0.31	0.11	-1.18
C4						0.13	0.33	0.13	-1.21
C5						0.16	0.36	0.16	-1.33
C6						0.15	0.35	0.11	-0.43
F2N	HR-ADCP	18	25	512 (@8 Hz)	900	0.10	0.18	0.06	0.41
F2S						0.08	0.16	0.08	0.44
F4N						0.10	0.18	0.10	0.65
F4S						0.10	0.18	0.10	0.58
F3N	ADV (Vector)	1	14	450 (@16 Hz)	900	0.22	0.06	0.09	0.60
F5N						0.21	0.05	0.11	0.57
F6N	ADV (Triton)	1	9	60 (@10 Hz)	90	0.13	0.13	0.13	0.59

^aHeight above bed to the centre of the measurement volume (point measurements) or the centre of the cell nearest to the bed (profile measurements)

below 70 counts were removed from the ADP and Triton ADV data (SonTek, 2000), whereas 50 counts was used as the threshold for all ADCP data (Nortek AS, 2017). Data with correlations less than 70% in the HR-ADCP and the vector ADV were discarded (Rusello et al., 2006). Filtered flow data were rotated from instrument to East–North–Up (ENU) coordinates, followed by computation of the total horizontal flow speed (U) and, for the flow profiles, the depth-averaged horizontal flow speed (U_{davg}). For the ADVs inside the forest, which only collected point data near the bed (Table 2), the near-bed flow speed was multiplied by a factor 1.3 for an estimation of the depth-averaged flow speed, following prior analyses of observed flow profiles on a mangrove platform (Horstman et al., 2015).

In situ pressure was corrected for atmospheric pressure variations, obtained from the meteorological station, and the temperature effect on pressure where possible. When instruments were exposed, temperature corrections were made using the linear relationship between the pressure anomaly and instrument-recorded temperature. Resulting pressure–temperature corrections varied between $+/-7.2 \cdot 10^{-3}$ to $1.1 \cdot 10^{-2}$ dBar per degree Celsius (i.e. $+/-0.72\text{--}1.1 \text{ cm}^{\circ}\text{C}$), plus a fixed offset ($+/-2.4 \cdot 10^{-2}$ up to $4.4 \cdot 10^{-1}$ dBar). Corrections resulted in water depth timeseries [$O(10^{-3})$ m] with an accuracy of $O(10^{-2})$ m. Additionally, pressure data of the continuously submerged ADP and ADCPs were corrected for fixed pressure offsets based on (i) prior and post-deployment out-of-water pressure offsets compared with the atmospheric pressure and (ii) the elevation of the water surface detected in the acoustic signal, defined as the cell with increased backscatter intensity (whilst accounting for the offset between the pressure sensor and the acoustic sensor). Lastly, water depths over each instrument were converted to local water levels by adding the bed level elevation as well as the height of the pressure sensor above the bed (Table 2).

For direct comparison of the flow and water level data obtained at different sampling durations and intervals, the ADV and HR-ADCP data were averaged over 90-s intervals (five intervals per burst), concurrent with the burst data of the remaining instruments. For the ADCP in the creek, as well as the ADP and the Triton-ADV, short-lived flow irregularities were removed by applying a 15-min moving average spanning ten consecutive bursts.

2.2.3 | Bulk drag coefficients

Tidal asymmetries in the creek and on the forest platform are caused by spatial variations in water level resulting from the combined effect of (i) decreasing propagation speeds of high and low tide up the creek system and (ii) frictional differences between the creek and the forest. Spatial gradients contributing to the along-creek momentum balance were computed in upstream direction (except at CO for the rising tide and at C6 for the falling tide for which we used downstream spatial gradients). We used the horizontal flow speed (U), which was nearly equivalent to the along-creek component of the velocity, in assessing the momentum balance, which was nearly equivalent to the along-creek component of the velocity (Figure 5). The inertial terms were two orders of magnitude smaller than the pressure gradient forcing, thus confirming the analytical scaling analysis of the momentum and continuity contributions in shallow funnel-shaped estuaries by

Friedrichs and Aubrey (1994). Neglecting the inertial contributions, the momentum balance then reduces to

$$g \frac{d\eta}{dx} = -\frac{\tau_{\text{bed+veg}}}{\rho h} = -C_D \frac{U|U|}{h}, \quad (3)$$

a balance between the water level gradient in the along-creek direction ($d\eta/dx$ [–]) and the combined friction losses due to bed roughness and vegetation drag ($\tau_{\text{bed+veg}}$ [N/m²]), where U is the local (depth-averaged) flow speed [m/s] and h is the local water depth [m]. These combined friction losses can be parameterised by a single bulk drag coefficient C_D [–] that incorporates the effects of grain and bedform roughness of the bed as well as the drag imposed by the vegetation (cf. Friedrichs, 2010). The balance in Equation 3 allows the bulk drag coefficient to be derived as the gradient of a linear fit through the water pressure gradient ($gd\eta/dx$) as a function of $U|U|/h$ (Mullarney et al., 2017b). Uncertain bed levels at the consecutive instrument stations due to survey inaccuracies ($O[10^{-2}\text{--}10^{-1}]$ m; see Section 2.1.1) will only cause a fixed offset of these linear fits. The accuracy of the resolved bulk drag coefficients depends on the temporal changes of local pressure differences only and, hence, is determined by the much higher resolution of the pressure gauges [$O(10^{-3})$ m; see Section 2.2.2].

The bulk drag coefficients obtained from the momentum fits according to Equation 3 comprise both energy losses due to bed shear stresses τ_{bed} and vegetation shear stresses τ_{veg} :

$$\tau_{\text{bed}} = \rho \frac{g}{C_{\text{bed}}^2} U|U| \text{ and} \quad (4)$$

$$\tau_{\text{veg}} = \frac{1}{2} \rho C_d N dh_{\text{veg}} U|U|, \quad (5)$$

respectively (Baptist et al., 2007). Herein, C_{bed} is the Chézy coefficient for the bed roughness [m^{1/2}s⁻¹], C_d is the dimensionless element drag coefficient of the vegetation and h_{veg} is the vegetation height [m]. Assuming bed roughness contributions on the mangrove platform were uniform across the study site and substituting from Equation (1), we obtain

$$C_D \propto C_d a h_{\text{veg}}, \quad (6)$$

the proportionality between the bulk drag coefficient and the canopy drag parameter $C_d a h_{\text{veg}}$. Herein, vegetation frontal surface area a [m⁻¹] was computed at each station using the vegetation survey data (Table 1). Vegetation height h_{veg} was assumed equal to the height of the pneumatophores since they contributed >90% of a . At every station, $a h_{\text{veg}}$ was then averaged with the value from the upstream station (seaward for rising tide, landward for falling tide), similar to the derivation of the spatial water level gradients.

3 | RESULTS

3.1 | Tidal propagation within the creek

The hydrodynamic observations covered relatively large (semidiurnal) spring tides of up to 1.9 m amplitude at the start of the data collection

period to relatively small neap tides of 1.0 m amplitude towards the end, measured at the estuary entrance near Whitianga (data obtained from NIWA Tide Forecaster: <https://tides.niwa.co.nz/>). Tidal stage-flow speed curves for the instrument stations along the thalweg of the creek displayed pronounced peaks in the observed depth-averaged flow speeds (Figure 2). Water levels at which maximum flood and ebb flow speeds occurred showed a consistent inland increase, controlled by the elevation of the banks along the creek (the overbank elevations in Figure 2) as well as the (mean) platform elevation of the surrounding forest (Figure 1d). At the seaward creek stations C0 and C1, flow speed maxima occurred at within-creek water levels for both ebb and flood. Conversely, at the inland creek stations C3–C6, both the ebb and flood flow speed maxima occurred at overbank elevations. At the creek entrance station C2, however, ebb flow maxima occurred mostly at within-creek water levels similar to the seaward stations, but maximum flood flow speeds occurred at overbank elevations similar to the landward stations (note the step change in the elevation of the yellow dots between C1 and C2 in Figure 2).

Maximum ebb flow speeds in the deeply incised inland section of the creek consistently occurred at water levels just above the bank level elevation, around the 10% platform elevation level ($\text{PLE}10 = 0.53 \text{ m} + \text{MSL}$; Figure 1d), regardless of changes in the tidal amplitude caused by spring-neap variations quantified by the high-tide water level (HWL) in Figure 3a. However, for rising tides, maximum flood flow speeds at these same stations occurred at systematically increasing water levels following increases of tidal amplitude (Figure 3b). Hence, in the confined inland sections of the creek (C3–C6), the ebb flow speed maxima occurred during the creek flow regime, when water levels were just exceeding the local bank level and a very limited part of the forest remained flooded (Figure 2); whereas the flood maxima were observed during the sheet flow regime, when water levels well exceeded the local bank levels, inundating large parts of the forest.

At the creek entrance (stations C1–C2), where the mangrove platform gives way to lower-elevation unvegetated tidal mudflats (Figure 1c,e), we observed a gradual transition from the creek-bound flow maxima at the seaward creek stations to the sheet-flow-related peaks in the flow speeds associated with inland stations (Figure 2). Ebb-tidal flow maxima at the creek mouth stations C1 and C2 were observed during the creek flow regime, and secondary velocity peaks

were present upon final drainage of the forest when water levels just exceeded the forest platform elevation. On the rising tide, the flow speed maxima at C1 occurred at the creek flow stage, while a secondary peak at the overbank stages was associated with the sheet flow stage inside the forest. At C2, this flood peak induced by the sheet flow over the forest platform was the largest, yet a secondary flood peak in flow speeds was evident during the creek flow stage, similar to the seaward stations.

The change of dominance and intensity of creek and sheet flow regimes along the length of the creek affected the amplitude and speed of the tide propagating in and out of the creek (Figure 4).

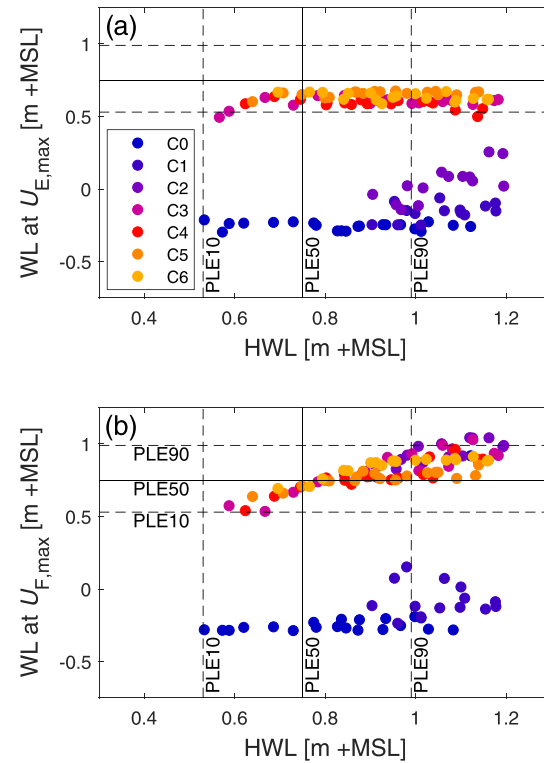


FIGURE 3 Water levels at the consecutive creek stations (a) at maximum ebb-tidal flow speeds and (b) at maximum flood-tidal flow speeds, both in relation to the local high-tide water level (HWL). PLE10/50/90 indicate the 10/50/90th percentiles of the platform elevation (Figure 1d) [Color figure can be viewed at wileyonlinelibrary.com]

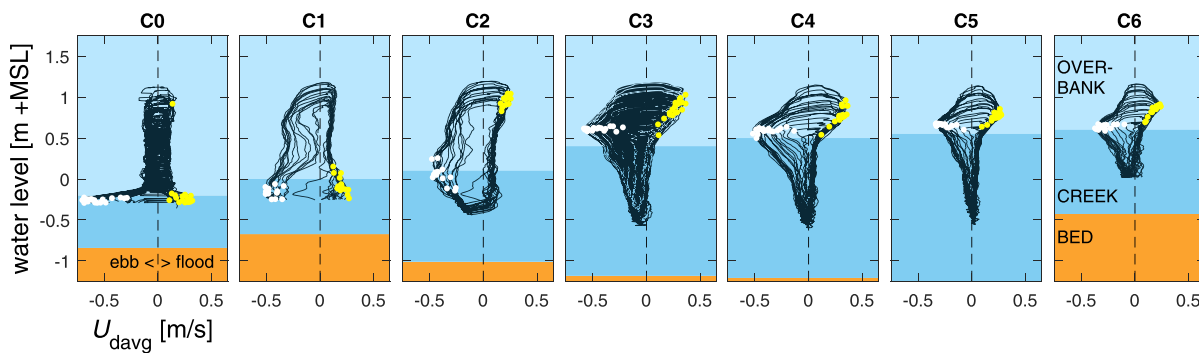


FIGURE 2 Tidal stage-flow speed curves for the depth-averaged flow speeds at the creek stations from the start (C0) to the end (C6) of the mangrove creek system (see Figure 1c for locations). Positive flow speeds are directed eastward, that is, flood tides, while negative flow speeds are directed westward, that is, ebb tides. Yellow and white dots on the stage-flow curves mark the flood and ebb flow speed maxima, respectively. Brown shading represents the creek bed, darker-blue shading represents the creek channel and the light-blue shading represents overbank elevations (the interface between the blue shades demarcates the local creek bank elevation) [Color figure can be viewed at wileyonlinelibrary.com]

Compared with the seaward station C0, the tidal amplitude (difference between high- and low-water levels) was amplified by about 10% at stations C1–C2 where the creek entered the forest (Figure 4b). While the tidal amplitude remained constant in the middle section of the creek (C3–C4), it showed a rapid drop towards the shallower creek end at C6. Every high tide (i.e. the crest of the tidal wave) generally propagated more quickly up the creek than the successive low tide (i.e. the trough of the tidal wave); thus, the timing delay between high and low tides (relative to the seaward station), and also the duration of the falling tide relative to the preceding rising tide, increased with distance inland (Figure 4c,d). Indeed, the rising tide at C6 caught up with the preceding falling tide, causing an elevated low tide water level at C6 compared with the more symmetrical tide at C0 (Figure 4a). This pattern in distortion varied across neap-to-spring tides (Figure 4d): When the high-water level remained below the mean platform elevation (HWL < PLE50), falling and rising tides were approximately equal in duration. However, for larger tidal amplitudes when substantial portions of the vegetated platform (HWL > PLE50) were flooded, distortions increased with tidal amplitude (Figure 4d). The maximum duration asymmetry was obtained when the tidal high-water level exceeded 90% of the platform elevation (HWL > PLE90), when falling tides at the most inland stations lasted 1.5–2 times longer than rising tides.

3.2 | Flow patterns and tidal asymmetries in creek and forest

Flow directions over the forest platform during the sheet flow stages of both flood and ebb tide were consistently creek-parallel, aligned

with the concurrent flow observations at the adjacent creek stations (Figure 5). The only exception was the creek-normal sheet flow at station F4N during the highest water levels, likely owing to a small local depression feeding a substantial area of the creek catchment in the northwest direction, that cannot flood from, or drain to, the estuary directly because of the raised ridge just inland of the forest fringe north of the creek mouth (see Section 2.1). Creek-normal flows on the vegetated platform are usually observed upon flooding and draining of the vegetated platform, at the end and start of the creek flow stage, respectively (Horstman et al., 2013; Temmerman et al., 2005). Such creek-normal flows over the forest platform were visually observed in the field at very shallow water depths but were not registered by the acoustic velocimeters and profilers that required minimum water depths of 20–30 cm to enable data collection (Table 2). At water depths >20–30 cm, both the inflow and outflow of the forest were characterised by sheet flow across the large-scale estuarine forest fringe (rather than the small-scale channel-fringe feature); the entire mangrove system floods from, and drains to, the seaward fringe of the forest, and mangrove forest surface elevations gradually increase inland from there. The average elevation of the forest platform between 100 m north and south of the creek increases from 0.0 m + MSL at transect 1 to 0.7 m + MSL at transect 6. This large-scale inland elevation change between the transects is greater than the bed level undulations along the individual transects across the forest platform (cf. Figure 1d).

Observed flow speeds within the forest were slower than the concurrent speeds at the adjacent creek stations, particularly during ebb (Figure 6a,b). Tidal asymmetries, quantified by the ratio of the maximum ebb to flood flow speeds during a tidal cycle, displayed opposite behaviour in the creek and forest: whereas flow speeds

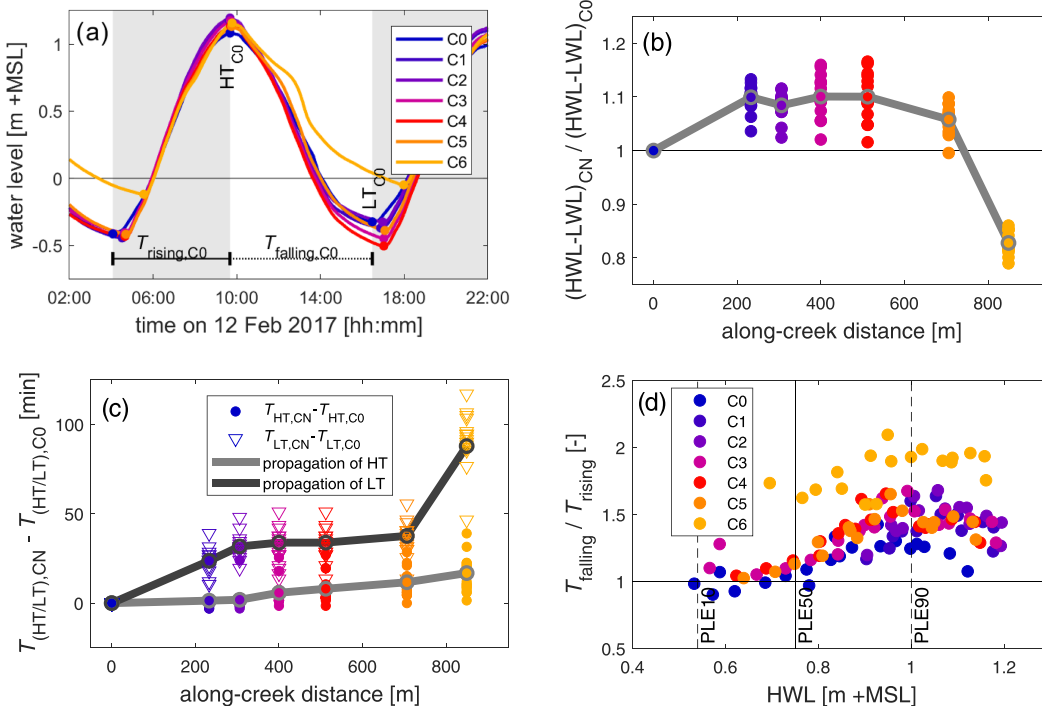


FIGURE 4 Tidal distortion at stations C0–C6 along the creek thalweg: (a) tidal water level variations along the creek during a single tidal cycle (HT = high tide; LT = low tide); (b) along-creek variation of the tidal amplitude (HWL = HT water level; LWL = LT water level), relative to the tidal amplitude at station C0; (c) along-creek delay of the arrival of high tide and low tide with respect to station C0; (d) tidal asymmetry at each station, expressed as the ratio of the duration of the falling tide relative to the preceding rising tide, for increasing high-water levels [Color figure can be viewed at wileyonlinelibrary.com]

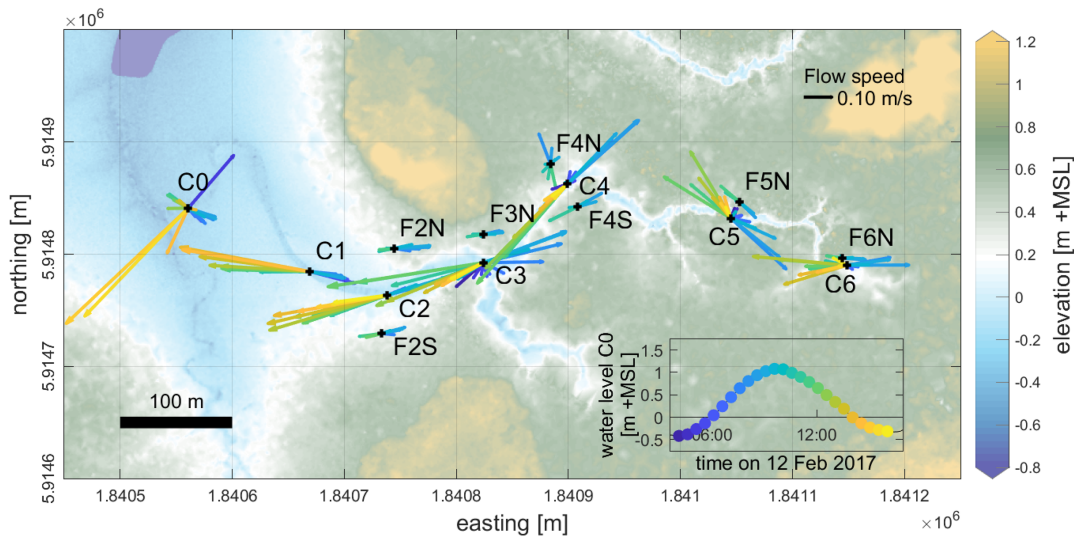


FIGURE 5 Map view of the changing orientation and magnitude of the depth-averaged tidal flow velocities within the creek and at the adjacent stations on the forest platform (velocity vectors are shaded in accordance with the colouring of the tidal stage curve in the inset) [Color figure can be viewed at wileyonlinelibrary.com]

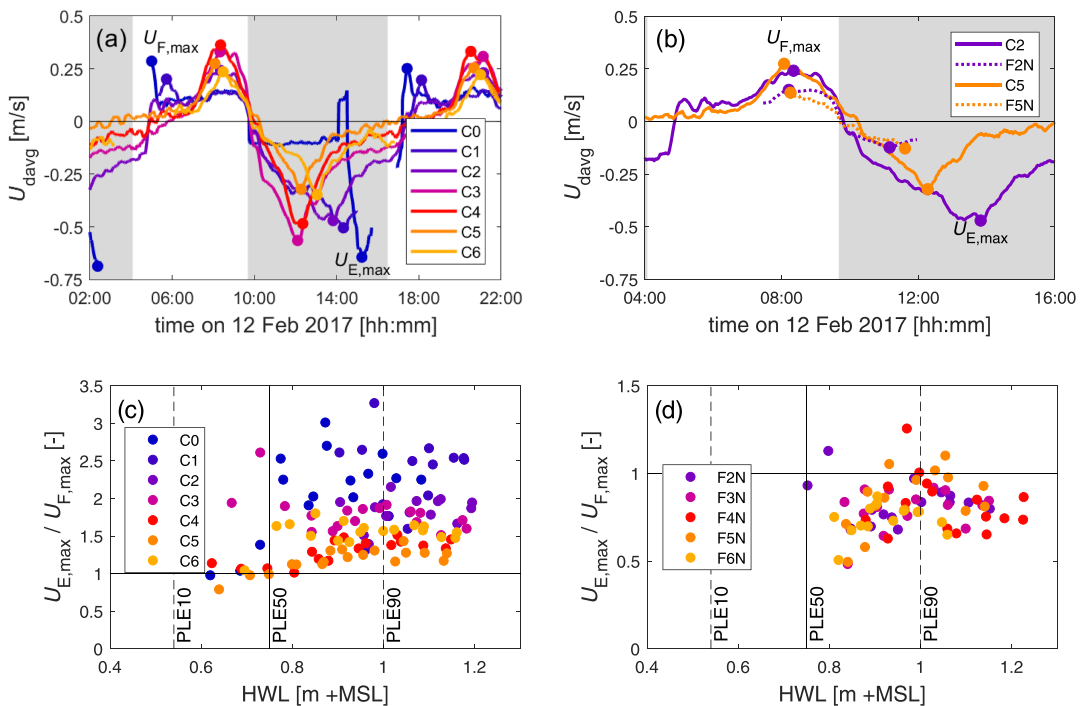


FIGURE 6 Maximum flood and ebb flow speeds in the creek and on the forest platform: fluctuations during a single tidal cycle at (a) the creek stations and (b) the creek and forest stations at transects C2 and C5. Tidal asymmetries, expressed as the ratio between the maximum ebb and flood flow speeds for (c) the creek stations and (d) the stations along the northern bank of the creek [Color figure can be viewed at wileyonlinelibrary.com]

within the creek were always ebb-dominant, flow speeds on the forest platform were consistently flood-dominant (Figure 6c, d). The ebb dominance in the creek gradually decreased with distance inland, concurrent with the declining size of the sub-catchment draining past these stations (Table 1). Similarly, ebb dominance at the creek stations increased slightly with tidal amplitude. This effect was mainly observed for high-water levels in the interval $PLE50 < HWL < PLE90$ (Figure 6c), when the flooded extent of the vegetated platform increased rapidly with the high-water level of the tide (Figure 1d). Above the 90% platform elevation threshold, the flooded extent of the forest platform only showed limited change with high-water levels and flow speed asymmetries remained more or less stable.

Conversely, the flood-dominant asymmetries within the forest showed a weak declining trend (the ratio in Figure 6d approaches 1) with high tide levels between the 50% and 90% platform elevations.

3.3 | Bulk drag coefficient changes with tidal stage

For each creek station, the bulk drag coefficient was resolved for every creek flow stage (below-bank water levels) and sheet flow stage (maximum flood-tidal flow speed until the consecutive maximum ebb-tidal flow speed) individually. Averaging over all tides then resulted in a single fit per tidal stage for each creek station (Figure 7a)

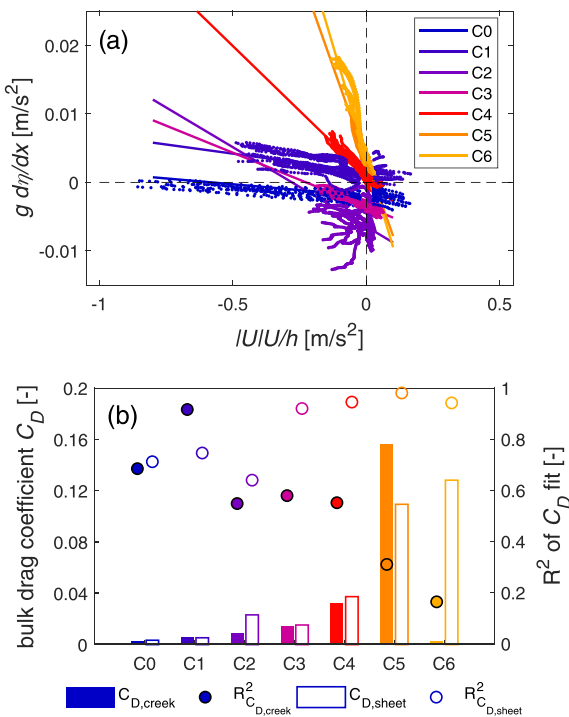


FIGURE 7 Bulk drag coefficients (C_D) at the creek stations: (a) bulk drag coefficients were obtained as the gradients of the linear fits to the water pressure gradient ($g d\eta/dx$) as a function of $U|U|/h$ for every tidal stage individually, which were then averaged over all tides; the example here shows the aggregated fits for the sheet flow stage, between the occurrence of maximum flood-tidal flow speed and the following maximum ebb-tidal flow speed at the creek stations. (b) Resulting bulk drag coefficients and R^2 values of the fits resolving C_D for both the creek flow stage and sheet flow stage at the consecutive creek stations [Color figure can be viewed at wileyonlinelibrary.com]

with a high goodness of fit at most stations (Figure 7b). The bulk drag coefficients increased substantially with distance inland for the creek flow stage, when the tide was below the bank level of the bare intertidal flats or the mangrove forest platform adjacent to the creek (at the seaward stations and further inland, respectively). The seaward creek stations C0 and C1 were positioned in a relatively shallow creek incising the surrounding unvegetated mudflats by 60–70 cm only (Table 1). At these seaward stations, the computed bulk drag coefficients were very small (0.003–0.006), representative of the coarse silts to medium sands on the creek bed (sediment samples had D_{50} of 33–480 μm) and the smooth surface of the (very) fine silts on the intertidal flats ($D_{50} = 6\text{--}10 \mu\text{m}$). Further inland, the creek formed a deep channel through the elevated mangrove forest platform, and the computed bulk drag coefficients for the creek flow stage increased from 0.009 at station C2 to 0.032 at station C4 (Figure 7b). This increase in bulk drag coefficients coincided with the presence of large irregularities in the profile of the creek, causing macro-scale bed roughness. Firstly, the creek displayed an increase in sinuosity with distance inland, with the position of the thalweg of the creek alternating between its banks (Figure 1b). Secondly, the creek narrowed with distance inland, and the banks of the creek became steeper and less smooth owing to closer proximity of the mangrove trees and roots that stabilised and protruded from the creek bank (the bank was sometimes undercut by erosion leaving a dense mat of exposed roots). Around station C5, where the creek was at its maximum depth but

also quite narrow, the creek banks were locally undercut, with the lateral roots of the mangroves holding together the overhanging surface layer of the forest platform (Figure 1f, Figures S3–S5). These lateral roots were likely the reason for the very large bulk drag coefficient of 0.156 obtained for station C5 during the creek flow stage.

Even though the upper layers of the flow in the creek were no longer confined within the hydraulically rough creek bed and banks during the sheet flow stage, we generally observed a steeper increase in the pressure gradient (relative to $U|U|/h$) along the creek thalweg during these overbank stages than during the creek flow stages at the inland creek stations. At stations C2–C6, the computed bulk drag coefficients were greater during the sheet flow stage than during the creek flow stage (Figure 7b). The only exception was station C5, where the computed bulk drag coefficient declined for tidal stages exceeding the level of the (overhanging) creek banks. Consequently, at the seaward creek stations C0 and C1, the computed bulk drag coefficients showed minimal to no change between the creek flow stage and the sheet flow stage (Figure 7b), as the bed roughness of both the creek and the surrounding unvegetated intertidal flats were similar.

Separating between the rising and falling legs of the sheet flow stage in the creek further improved the fits that resolved the bulk drag coefficient (see the R^2 values in Table 3). During the sheet flow stage, observed drag coefficients on the rising tide exceeded those during the falling tide at the seaward creek stations (C0–C3), but at the inland creek stations (C4–C6) the drag coefficients were larger during the falling tide (Table 3). This change between stages coincided with the transition from an increasing to a decreasing tidal amplitude that was observed between the seaward and landward parts of the creek (Figure 4b). These results also corroborated the gradual decline of the ebb dominance of the flow speeds at the creek stations further inland as observed in Figure 6c; the smaller bulk drag coefficients are associated with faster flow speeds at the seaward stations during the falling tide and at the landward stations during the rising tide.

Applying the same procedure to the observations at the stations on the forest platform provided concurrent bulk drag coefficients within the mangrove vegetation during rising and falling tide, with equally good fits (Table 3). Drag coefficients within the forest were consistently smaller on rising tide than during falling tide, promoting the observed flood dominance of the flow speeds within the forest (Figure 6d). Notably, during rising tide, the drag coefficients computed for the forest were similar to, or less than, the values computed for the adjacent creek station, except at the most inland station. For falling tides, the obtained drag coefficients at the forest stations F2 and F3 were greater than those at the adjacent creek stations.

3.4 | Bulk drag coefficient changes with vegetation density

The bulk drag coefficients computed for the sheet flow stages at both the forest and creek stations were found to correlate well with the vegetation solid volume fraction in the respective sections of the mangrove forest, particularly for the falling tide. There was a weak, but not significant, negative correlation of the bulk drag coefficients in the forest and the dimensionless vegetation frontal surface area ah_{veg} ($r = -0.33$, $p = 0.35$; Figure 8a). A much stronger and

TABLE 3 Computed bulk drag coefficients (C_D) and accompanying R^2 values (between brackets) of the linear fits used to resolve C_D (Figure 7a). Values presented for the full creek flow stage at all creek stations (below-bank water levels) and the full sheet flow stage at both the creek and forest stations (here the period between the occurrence of maximum flood flow speed and the following maximum ebb flow speed at the creek stations, or the full inundation period for the forest stations), as well as for the rising (flood) and falling (ebb) legs of the sheet flow stages at the creek and forest stations

Creek flow stage		Sheet flow stage			Sheet flow stage			
Total		Total	Flood	Ebb		Total	Flood	Ebb
C0	0.003 (0.68)	0.003 (0.71)	0.013 (0.86)	0.003 (0.96)	-	-	-	-
C1	0.006 (0.92)	0.005 (0.75)	0.024 (0.89)	0.006 (0.85)	-	-	-	-
C2	0.009 (0.55)	0.023 (0.64)	0.020 (0.80)	0.017 (0.57)	F2N	0.027 (0.50)	0.023 (0.15)	0.041 (0.52)
C3	0.015 (0.58)	0.015 (0.92)	0.057 (0.93)	0.012 (0.86)	F3N	0.070 (0.91)	0.039 (0.67)	0.051 (0.92)
C4	0.032 (0.55)	0.037 (0.95)	0.020 (0.91)	0.041 (0.98)	F4N	0.023 (0.88)	0.018 (0.78)	0.033 (0.82)
C5	0.156 (0.31)	0.109 (0.98)	0.031 (0.80)	0.119 (0.97)	F5N	0.031 (0.91)	0.018 (0.78)	0.075 (0.77)
C6	0.003 (0.16)	0.128 (0.94)	0.065 (0.92)	0.145 (0.91)	F6N	0.098 (0.81)	0.078 (0.87)	0.128 (0.68)

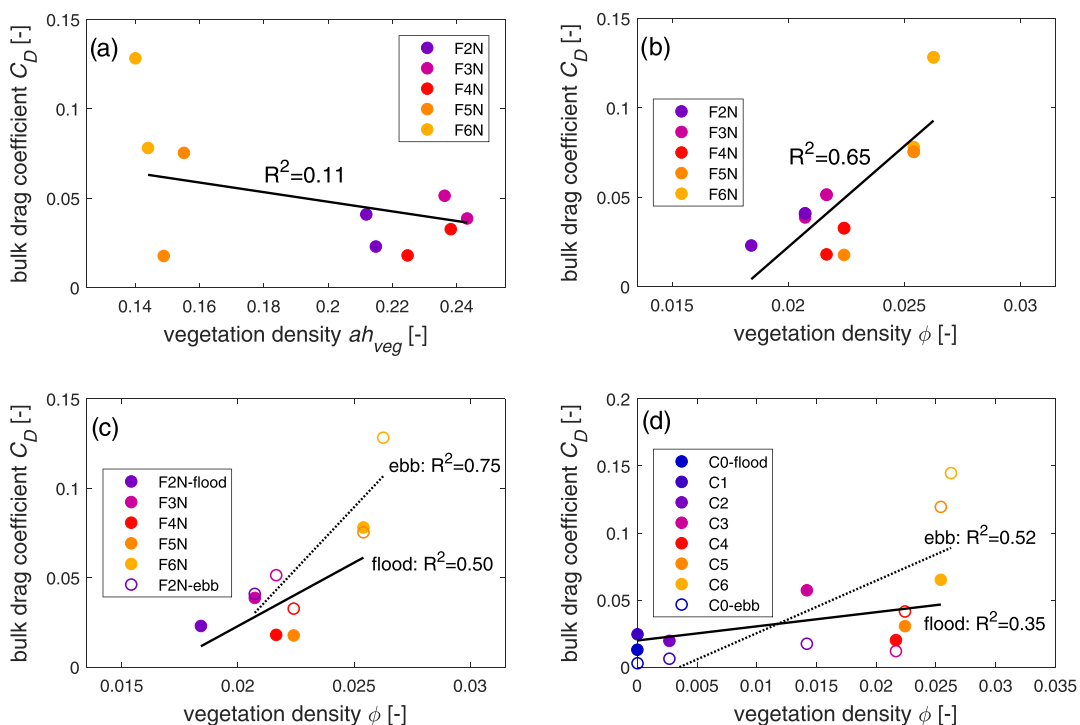


FIGURE 8 Correlations of the computed bulk drag coefficients during the sheet flow stage with the vegetation density: (a) bulk drag coefficients in the forest as a function of the dimensionless vegetation frontal area density ah_{veg} and (b) as a function of the vegetation solid volume fraction ϕ ; (c) linear fits of the ebb and flood bulk drag coefficients in the forest as a function of ϕ ; and (d) linear fits of the ebb and flood bulk drag coefficients along the creek as a function of ϕ at the adjacent forest stations (or the adjacent creek bank at C1 and bare mudflat at C0; Table 2). In (c,d) the sheet flow stage is subdivided in the rising tide (flood) and the falling tide (ebb), as in Table 3 [Color figure can be viewed at wileyonlinelibrary.com]

significant correlation was obtained by substituting the dimensionless frontal vegetation surface area with the dimensionless vegetation solid volume fraction ϕ (Table 2), which equates to the planar vegetation surface area. The bulk drag coefficients at the forest stations showed a significant positive correlation with ϕ ($r = 0.81$, $p < 0.01$; Figure 8b). Sheet flow bulk drag coefficients for the creek also strongly correlated ($r = 0.63$, $p = 0.02$) with the vegetation density ϕ on the adjacent forest platform (substituted with values from the adjacent creek banks and bare mudflat at C1 and C0, respectively). The correlation between the bulk drag coefficients and the vegetation density was stronger for falling tides than for rising tides during the sheet flow stage, in the forest (Figure 8c) as well as in the creek

(Figure 8d). The enhanced energy losses during falling tide, associated with the greater bulk drag coefficients, were caused by enhanced water level gradients during falling tides at the inland (creek) stations.

4 | DISCUSSION

4.1 | Quantifying the impact of vegetation on the mangrove platform

The lack of correlation between the calculated bulk drag coefficients and the dimensionless vegetation frontal surface area ah_{veg} in the

forest, as observed in Figure 8a, possibly stemmed from the variability of the element drag coefficient C_d in Equation 6 in combination with the declining height of the pneumatophores with distance inland (Table 1). The element drag coefficient is known to decline with increasingly turbulent flow conditions (increasing Reynolds number), but also depends on vegetation properties (Mullarney & Henderson, 2018). Based on a range of experimental studies with emergent artificial canopies, Nepf (1999) showed that the element drag coefficient decreased with increasing canopy density, quantified as ad ($ad = Nd^2 \propto \phi$). Moreover, experiments with submerged canopies of natural mangrove pneumatophores showed the element drag coefficient to increase with submergence ratios h/h_{veg} but to be largely unaffected by the vegetation density (Horstman et al., 2018a). In the present study, the relative decline in height of the pneumatophores at the inland forest stations was greater than the relative increase of their frontal surface area a (Table 1), causing ah_{veg} to decline with distance inland. The inland reduction in the pneumatophore height was greater than the change in water depth at the consecutive forest stations, as bank levels were relatively constant along the inland creek extent (Table 1) and along-creek water level differences were also relatively small (Figure 4a). The submergence ratio h/h_{veg} increased from about 5 to 11 between stations F3 and F6 (station F2 showed intermediate ratios). The combination of the smaller frontal surface area and the larger submergence ratio of the pneumatophore canopy with distance inland are both indicative of a corresponding inland increase of the element drag coefficient C_d . An increasing value inland of the element drag coefficient could have resulted in the negative correlation between the bulk drag coefficient C_D and the vegetation frontal density ah_{veg} in Figure 8a.

Following the strong positive correlation between the bulk drag coefficient and the vegetation solid volume fraction ϕ (Figure 8b), we argue that the vegetation solid volume fraction may provide an improved estimator for vegetation-induced drag compared with the frontal surface area. A direct correlation between bulk drag and the vegetation solid volume fraction was also observed in previous experimental work with real pneumatophore canopies (Horstman et al., 2018a), as well as mimic canopies of *Rhizophora* mangrove stilt roots (Maza et al., 2019). Experimental studies with mimic canopies covering a range of stem diameters d and stem densities N have shown that vegetation drag as well as sediment resuspension collapse for morphologically different canopies (different d and N) with the same solid volume fraction (Tinoco & Coco, 2016; Tinoco & Cowen, 2013).

4.2 | Impacts of a vegetated mangrove platform on within-creek dynamics

Although no vegetation was present within the confined width of the creek channel, we found that the bulk drag coefficients for the sheet flow stage in the inland section of the creek were substantially altered by the presence of the mangroves on the adjacent forest platform. Bulk drag coefficients for both the rising and falling parts of the sheet flow stage at the creek stations (Table 3) showed a significant and strong positive correlation with the coefficients derived for the adjacent forest stations ($r = 0.86$, $p < 0.01$). However, the correlation between the bulk drag coefficients at the creek stations for the sheet

flow stage and the creek flow stage (Figure 7b) was non-significant. This result indicates that, during the sheet flow stage, the pressure gradient along the creek thalweg was impacted more substantially by the along-creek pressure gradient over the surrounding mangrove platform (arising from the total roughness) than by the hydraulic roughness of the creek bed itself. Hence, the interaction between forest platform and the creek imposes the steeper increase in the pressure gradient (relative to $U|U|/h$) along the creek thalweg during the sheet flow stage. Interestingly, the sheet flow bulk drag coefficients at the forest stations were not consistently greater than at the adjacent creek stations (Table 3). This similarity in coefficients could be due to the moderate mangrove density on the forest platform (Table 1) only partially compensating for the relative smoothness of the forest floor compared to the hydraulically rough planform of the creek channel (C_D represents friction losses due to both vegetation drag and bed roughness). Similarly, previous field studies have shown that the faster speed of the tidal current in the deeper low-resistance creeks increases flow speeds on the adjacent vegetated creek banks (Horstman et al., 2013; Mazda et al., 2005) and can cancel, or reduce, cross-shore (i.e. fringe-normal) water level gradients on the forest platform during the sheet flow regime (Montgomery et al., 2018).

Steepening water level gradients in the creek and the associated greater bulk drag coefficients showed that the vegetated forest platform had a much greater impact on the within-creek hydrodynamics during the sheet flow stage than would typically be assumed in numerical studies of such interactions between a creek and its surrounding vegetated platform. The bulk drag coefficient from Equation 3, which combines energy losses due to both bed shear stresses and vegetation drag (Equations 4–5), equates to the Chézy roughness coefficient C [$m^{1/2}s^{-1}$] for the total hydraulic roughness according to

$$\tau_{bed+veg} = \rho C_D U|U| = \rho \frac{g}{C^2} U|U| \quad (7)$$

Following Equation (7), the observed inland increase of the bulk drag coefficients at the creek stations during the sheet flow stage (Table 3) equates to a decline of the total Chézy coefficient from 40 to 60 [–] at the creek mouth (stations C0 and C1) to values of 10–30 [–] for the deeply incised sections of the creek. This latter range was similar to the Chézy values of 10–20 [–] that we obtained at the forest stations during sheet flow conditions. The hydraulic roughness observed at the creek mouth stations, where the channel was relatively shallow and surrounded by low-elevation unvegetated intertidal flats, was typical for the sediment grain sizes of the bed (see Section 3.3). The hydraulic roughness experienced in the deep inland sections of the creek that incise the vegetated mangrove platform was substantially larger. At these inland sections, mangrove roots allowed for cliff formation and undercutting of the banks, and roughness values were comparable to those within the surrounding vegetated forest platform during sheet flow stages.

Thus, for accurate simulations of the landscape-scale feedbacks between the creek and the surrounding mangrove forest, it is essential that the creek bed roughness represents both the direct and indirect contributions of mangrove vegetation, through undulated/overhanging creek banks and modulated friction of overbank sheet flows, respectively. Previous numerical modelling studies of the interactions between a creek channel and its surrounding vegetated

platform assumed Chézy values as small as 1–5 for vegetated mangrove platforms (Mazda et al., 1995) and 10–20 on salt marsh platforms (Stark et al., 2015), whereas values of 61 and 55–75 were assumed for the creek channels through these ecosystems, respectively. Although our observations of the hydraulic roughness at the creek mouth (stations C0–C1) were in agreement with the values assumed in the numerical studies mentioned above, the roughness we observed in the deeply incised creek channel (at stations C2–C6) was substantially larger, more similar to the roughness on the forest platform. The roughness we observed within the mangrove vegetation at our study site was somewhat lower than in these numerical studies. However, Mularney et al. (2017b) observed bulk drag coefficients of 0.041–0.18 across a dense mangrove fringe in Vietnam, declining to 0.019–0.032 in the sparser inland mangrove forest, similar to the range of the results in this study (Table 3).

4.3 | Creek flow and sheet flow interactions: The effect on tidal asymmetry

Apart from the contribution of the vegetation to the observed hydrodynamics in the creek during the sheet flow stage, the morphology of the creek and the surrounding platform imposed a direct relationship between tidal flow maxima and the tidal prism. Established power-law scaling relationships exist between the channel area, the maximum discharge and the tidal prism of tidal channel networks (D'Alpaos et al., 2010; Rinaldo et al., 1999b). Here, we obtained a strong power-law relationship between the maximum ebb-tidal depth-averaged flow speed at each creek station and the tidal prism of the inland sub-catchment ($R^2 = 0.70$; Figure 9a):

$$U_{E,\max} \propto P_{CN}^{0.28}, \quad (8)$$

where P_{CN} is the tidal prism [m^3] of the sub-catchment inland of creek station CN, assuming a uniform maximum water level equal to the high tide water level at station CN for each tide. The scaling coefficient in Equation 8 was combined with the scaling coefficient of the power relationship for the channel cross section $\Omega \propto P^{6/7}$ (D'Alpaos et al., 2010) to compute the scaling coefficient of the maximum discharge ($Q = U\Omega$). We obtained a scaling coefficient for the maximum discharge in relation to the tidal prism that is close to the unity value that Rinaldo et al. (1999b) found with their empirical-analytical relationships. The strength of the scaling relationship between the ebb flow speed maxima and the tidal prism is linked to the consistent timing of these maxima when the tide drops below the bank level of the forest platform (Figure 3a). The falling tide in the catchment decouples from the offshore tide when it drops below the platform elevation, causing the momentum balance to become essentially fluvial, that is, balancing the pressure gradient with friction as in Equation 3 (Speer et al., 1991). Scaling relationships between channelisation, catchment area and slope generally apply in such fluvial systems (Montgomery & Dietrich, 1992; Rinaldo et al., 1999a). Maximum flood flow speeds lacked a clear scaling relationship with the tidal prism (scaling coefficient = 0.10, $R^2 = 0.17$; Figure 9b) because the tidal stage at which these speeds occurred increased with the maximum water level instead of being fixed at the bank level of the creek (Figure 3b). In contrast to the maximum ebb flow speeds, the

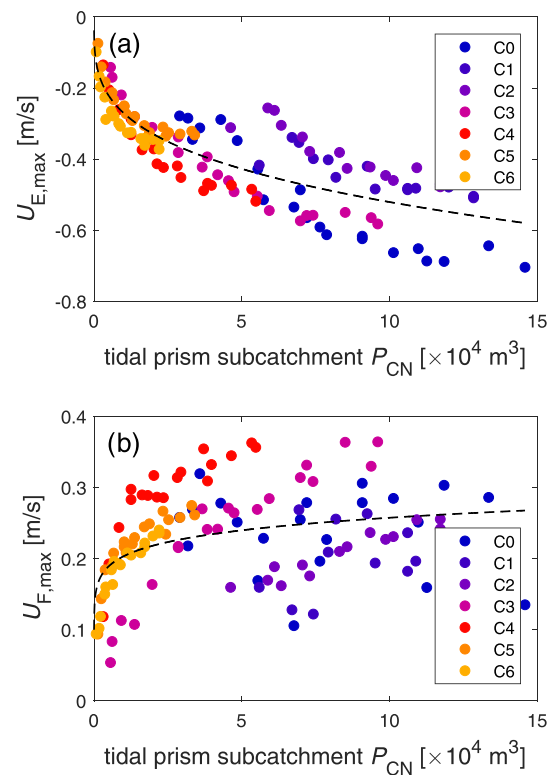


FIGURE 9 Maximum depth-averaged flow speeds at the consecutive creek stations followed a power-law relationship with the tidal prism of the sub-catchment P_{CN} upstream of station CN (assuming a uniform maximum water level throughout the sub-catchment equal to the high tide water level at station CN): (a) maximum ebb flow speeds showed a clear power law relationship with a scaling coefficient of 0.28 ($R^2 = 0.70$); (b) maximum flood flow speeds related weakly to the tidal prism of the upstream sub-catchment with a scaling coefficient of 0.10 ($R^2 = 0.17$) [Color figure can be viewed at wileyonlinelibrary.com]

maximum flood flow speeds occurred during the sheet flow stage. Consequently, confounding effects of the spatially variable bed and vegetation roughness of the forest platform on the maximum flood flow speeds within the creek affected the scale-invariant scaling relationship with the tidal prism (Rinaldo et al., 1999a).

The occurrence of flood and ebb flow speed maxima during the sheet flow stage and the creek flow stage, respectively, caused substantial velocity asymmetries between the rising and falling tide. As with any shallow water wave, the greater impact of the bottom roughness at lower water depths caused the propagation speed of low tides along the creek to reduce with distance inland more quickly than the propagation speed of high tides (Figure 4c). The resulting duration asymmetry of the tidal wave (Figure 4d) is an effect that dominates in convergent tidal basins with small intertidal platforms (Friedrichs, 2010; Friedrichs & Aubrey, 1988). The shorter rising tide is normally associated with stronger flow speeds (i.e. flood dominant) to maintain continuity (Friedrichs & Aubrey, 1988). However, we consistently observed greater maximum flow speed during ebb tides, thereby creating ebb-dominant conditions in the creek (Figure 6c). This atypical ebb dominance in the creek is caused by the creek-parallel flows over the forest platform during the sheet flow stage (Figure 5). Therefore, these consistent creek-parallel flows invalidate the common assumption that the intertidal platform simply functions as storage, while mass and momentum are exclusively transported

through the creek channel (Friedrichs, 2010; Friedrichs & Aubrey, 1988; Rinaldo et al., 1999b; Speer et al., 1991). Hence, while ebb flow speed maxima in the creek were observed during the creek flow stage (Figure 2), when transport of mass and momentum were indeed confined to the creek, flood flow speed maxima in the creek occurred during the sheet flow stage (Figure 2) and were slower owing to the combined transport through the creek and over the forest platform. The flood-dominant velocity asymmetry on the forest platform (Figure 6d) contributed to this reduction of the flood flow speed maximum within the creek.

The observed flow speed and duration asymmetries between rising and falling tides along the creek channel were the combined effect of both the large-scale hypsometry and the vegetation properties in relation to the tidal stage, while local variations in the slope and geometry of the creek bed only generated minor variation in these asymmetries. All creek stations were found to be ebb-dominant in terms of flow speed (Figure 6c), despite the potential flow deceleration by the upward slope of the creek bed in the seaward direction in the middle section of the creek (between stations C5 and C1; Table 1). The increasing roughness of the creek bed with distance inland (Table 3) limited the maximum ebb flow speeds, which occurred during the creek flow stage. The contribution of vegetation on the mangrove platform to the total roughness increased the bulk drag coefficients at the inland parts of the creek during the sheet flow stage (Table 3) and, consequently, reduced the flood flow speed maxima in the creek. During overbank tides with high-water levels between the mean and 90% platform elevation marks, these sheet flow dynamics resulted in a gradual inland decline of the ebb flow speed dominance (Figure 6c) but an increase of the falling tide duration, which reached twice the rising tide duration at the landward end of the creek (Figure 4d). For spring tides that exceeded 90% platform elevation, the velocity asymmetry remained mostly constant (Figure 6c), with a small decline in relative duration of the falling tide, particularly at the creek mouth (station C0; Figure 4d). The asymmetric shape of the tidal stage-flow speed curves at the inland section of the creek (stations C3–C6; Figure 2), as well as the observed longer falling tides and the ebb dominance of the flow speed maxima at all creek stations, is an established characteristic of tidal channel flow in intertidal mangroves and salt marshes (e.g. Bayliss-Smith et al., 1979; Mazda et al., 1995; Pethick, 1980). Similar to our results, Stark et al. (2015) observed a relative increase of the duration of the falling tide (up to 2.5 times longer than the rising tide) throughout a salt marsh creek system for overbank tides, while at the marsh edge this duration asymmetry declined once the tide flooded almost all of the platform ($HWL > 90\%$ platform elevation). The relatively limited extent of our study site probably limited the further increase of the duration of the falling tide in the inland direction, a trend that Stark et al. (2015) did observe for the highest spring tides.

4.4 | Creek flow and sheet flow interactions: The effect on high-water level reduction

Local water level gradients at the creek and adjacent forest stations were moderated by along-creek changes in the amplitude of the tidal wave as it propagated into the mangrove forest system. Following the analytical results of Friedrichs and Aubrey (1994) for tidal propagation

in strongly convergent shallow estuaries, the growth of the tidal amplitude at the creek mouth (between stations C0–C1) was attributed to the shoaling of the tidal wave due to the decreasing channel dominating over the local increase of the total transect width. Additionally, the elevation of the surrounding intertidal flats at the creek mouth gradually increased towards the mangrove fringe (Figure 1c), contributing to the shoaling effect. In the seaward section of the creek (between stations C1 and C4), tidal amplitudes were approximately constant; here, the continued shoaling due to the gradual inland increase of the height of the banks and forest platform surrounding the creek was likely offset by the amplitude-reducing effect of the flow divergence due to the gradual inland increase of creek depth and platform width (Table 1; Figure 2). Conversely, the tidal amplitude decayed in the landward section of the creek (between stations C4 and C6; Figure 4b), due to the frictional effects of a (narrowing) vegetated platform dominating over the amplifying effect of the reducing creek depth (Friedrichs & Aubrey, 1994; Friedrichs & Madsen, 1992). Another factor contributing to the reduction of the tidal amplitude was the incomplete drainage of the falling tide at the inland creek end (station C6; Figure 4a), which substantially elevated the minimum water level at low tide.

The ability of mangroves to reduce flood hazards relates to the reduction of the highest water level and not the amplitude of the tide; a substantial yet spatially variable reduction rate was observed throughout the study site, which was substantially greater over the forest platform than along the creek. At the mouth of the creek system (between stations C0 and C1), shoaling of the tidal wave caused high-water levels to increase at a rate of up to 60 cm/km (Figure 10a). Once the creek entered the forest and formed a deep channel cutting through the mangrove platform (inland from station C1), high-water levels at the consecutive creek stations were consistently lowered (Figure 10a). Reduction rates of the tidal high-water levels had a maximum of up to 43 cm/km along the seaward section of the creek (between stations C1 and C3/C4), but gradually declined inland to a maximum of 9 cm/km along the full length of the creek (between stations C1 and C6). Comparing the high-water levels at the mouth of the creek system with those over the forest platform, we observed a maximum reduction rate of up to 95 cm/km across the forest fringe (between stations C1 and F2N) that again declined inland to a maximum of 27 cm/km across the full extent of the forest (between stations C1 and F6N; Figure 10b). The atypical amplification rates for station F4N may be associated with anomalous dynamics at this station associated with a local depression, feeding a substantial section of the northwest of the creek catchment (see Section 3.2). Notably, the reduction rates in Figure 10 were computed with the along-creek distance between instrument stations. If substituted with the straight-line distance between stations, the total reduction rate along the full length of the creek increased to 12 cm/km, whereas over the forest platform the reduction rate increased to a maximum of 36 cm/km between the mouth of the creek and the most inland station on the forest platform.

The attenuating capacity of the mangrove forest is substantially reduced by the presence of the creek, as evidenced by both the difference in reduction rates between the creek and the forest platform as well as the computed bulk drag coefficients. Our results clearly demonstrated a correlation between water level gradients along the course of the creek and the enhanced roughness due to the mangrove

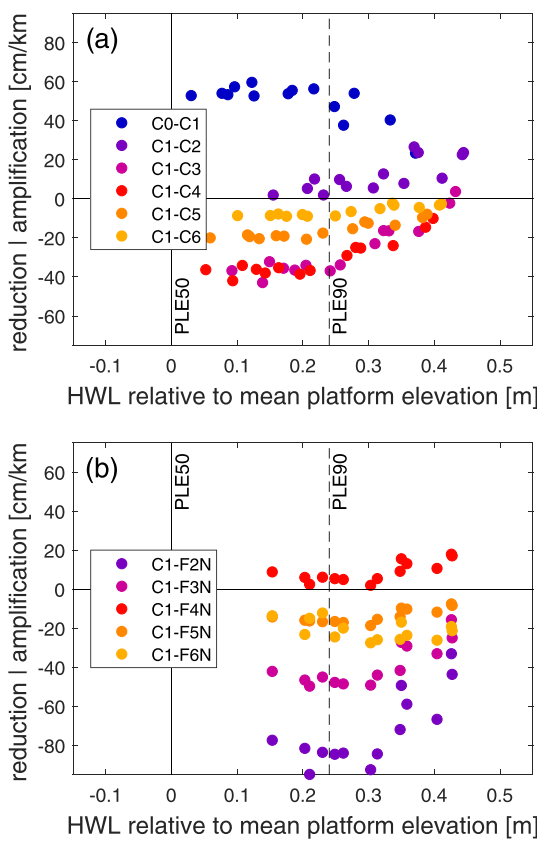


FIGURE 10 Reduction (negative) and amplification (positive) rates of the tidal high-water levels at the consecutive inland stations compared with the high-water level at station C1 at the mouth of the creek for (a) the creek stations and (b) the stations on the forest platform. These rates were computed as the difference between the maximum tidal water levels at the stations (these levels do not necessarily coincide in time), divided by the along-creek distance between the respective stations. Maximum water levels at high tide (HWL) on the horizontal axis are relative to the mean platform elevation (PLE10/50/90 indicate the 10/50/90th percentiles of the platform elevation; Figure 1.d) [Color figure can be viewed at wileyonlinelibrary.com]

vegetation on the forest platform (Section 3.4). However, it was not possible to isolate the decrease in the reduction rates across the forest platform, because of the impact of enhanced flow through (and hence smaller reduction rates along) the hydraulically smooth creek. For comparison, in a nearby mangrove forest in New Zealand without creeks dissecting the forest platform, a 24 cm/km attenuation rate was observed during a storm surge with a 10-year return period (Montgomery et al., 2019). This value is similar to the total reduction rate we obtained between the mouth of the creek and the most inland station on the forest platform, with the presence of a creek. This result is in contrast to the lack of high-water level reduction observed in creek-dissected mangroves at Pahoia, Tauranga Harbour (Montgomery et al., 2018). However, the mangrove vegetation at Pahoia was much more stunted (i.e. lower height) than at the present field site, due to increasing temperature stresses further south (Horstman et al., 2018b). At Pahoia, the submergence of stunted mangrove canopies during high tide likely reduced the sheet flow contribution of the forest platform, limiting the contribution of the mangrove vegetation to the bulk drag coefficients in the creek at overbank stages and reducing the attenuation of the tidal wave.

The reduction rates of high-water levels across the forest platform, especially across the forest fringe, were greater than previously observed rates in coastal wetlands, although they declined for increasing high-water levels. The observed system-wide reduction rates were of the same order of magnitude as previously observed attenuation rates of 4–25 cm/km for (hurricane-induced) storm surges over vast stretches of salt marshes and mangroves (Krauss et al., 2009; Wamsley et al., 2010). Our observed reduction rates were up to one order of magnitude greater than the maximum reduction rate of 4 cm/km that was obtained by Stark et al. (2015) for the high-water level reduction along a salt marsh channel network. In their salt marsh study, reduction rates in the channel were found to increase with increasing high-water levels up to the 90% platform elevation level, and above this level reduction rates were reduced (and even turned into an amplification rate during a storm tide). In our study, for high tides exceeding the 90% platform elevation, we similarly observed a rapid decline of the reduction rates, both along the creek and in the forest. This observed decline of the reduction rate with distance inland matches well to the diffusion model that Montgomery et al. (2019) derived analytically for the propagation of surges in mangroves. However, observations presented in the present study largely omitted the potential contribution of the tree canopies to the attenuating drag forces, as the tall mangrove canopy remained emergent during normal high tide conditions. Submergence of the denser canopy of the trees under extreme storm surge conditions would likely dramatically increase the vegetation drag and hence the attenuation rate.

5 | CONCLUSIONS

We presented a high-resolution data set of tidal water levels, flow speeds, and morphological and vegetation properties along the full length of an intertidal mangrove creek system, both for the creek and the vegetated platform. Asymmetry and attenuation patterns in the creek and the forest were explained by considering differences between creek and sheet flows, properties of the vegetation and morphology, and associated bulk drag coefficients.

We observed that the duration of the falling tide in the creek channel was longer and increased inland, associated with an ebb-dominant velocity asymmetry that decreased inland. The ebb flow speed maxima within the creek, strictly occurring during the creek flow stage, obeyed a power-law scaling relationship with the tidal prism that is characteristic of tidal channel networks dissecting intertidal (vegetated) platforms. This scaling relationship was much weaker for maximum flood flow speeds in the creek, due to their occurrence during the sheet flow stage and a substantial contribution of mass and momentum transport over the forest platform.

Bulk drag coefficients were found to vary along the creek and were different between tidal stages. In the forest, bulk drag coefficients displayed a significant positive correlation with the planar vegetation density. The mangrove vegetation on the vegetated platform was found to contribute to the tidal dissipation in the creek during the sheet flow stage, shown by the significant positive correlation of the bulk drag coefficients computed for the creek stations with the bulk drag coefficients of the adjacent forest. Accordingly, the slower flood-dominant sheet flows over the vegetated mangrove platform

reduced the concurrent flow speeds within the creek. Greater bulk drag coefficients during falling tides caused a convergence of the faster *ebb-dominant* creek flows within the deeply incised creek.

Consistent with the inland increase in bulk drag coefficients along the creek, we observed reduction rates of tidal high-water levels up to 12 cm/km between the creek mouth and the end of the creek channel. Reduction rates in the forest were higher, up to 36 cm/km along the full creek length. These reduction rates as well as the bulk drag coefficients observed within the creek were strongly moderated by the vegetation on the forest platform. These findings emphasise that the forest platform is not simply a place to store water; rather, there are strong dynamical links between the creek and the surrounding mangrove forest. Therefore, applied studies on, for example, the use of natural mangrove systems for coastal defence purposes should be based on a full-system approach.

ACKNOWLEDGEMENTS

This research is funded by the Royal Society of New Zealand's Marsden Fund (grant 14-UOW-011). We thank Steve Henderson, Dean Sandwell, Hieu Nguyen and John Montgomery for their contributions and for field assistance. We thank two anonymous reviewers and the editor for their constructive feedback.

CONFLICT OF INTEREST

The authors declare that there are no conflicts of interest.

DATA AVAILABILITY STATEMENT

The data that support the findings of this study are available from the corresponding author upon reasonable request.

NOTATION

a	vegetation frontal area density [m^{-1}]
ah_{veg}	frontal vegetation surface area [—]
C_{bed}	Chézy bed roughness coefficient [$\text{m}^{1/2} \text{s}^{-1}$],
C_d	vegetation element drag coefficient [—]
C_D	bulk drag coefficient [—]
d	vegetation diameter [m]
D_{50}	mean sediment grain size [μm]
g	gravitational acceleration [m/s^2]
h	water depth [m]
h_{veg}	vegetation height [m]
HWL	high-tide water level [m + MSL]
N	vegetation stem density [m^{-2}]
P_{CN}	tidal prism of the sub-catchment upstream of creek station CN [m^3]
PLE10	10th percentile of the platform elevation (0.53 m + MSL)
PLE50	50th percentile of the platform elevation (0.75 m + MSL)
PLE90	90th percentile of the platform elevation (0.99 m + MSL)
Q	creek discharge [m^3/s]
U	total horizontal flow speeds [m/s]
U_{davg}	depth-averaged horizontal flow speed [m/s]
$U_{\text{E,max}}$	maximum ebb-tidal depth-averaged flow speed [m/s]
$U_{\text{F,max}}$	maximum flood-tidal depth-averaged flow speed [m/s]
$d\eta/dx$	water level gradient in the along-creek direction [—]
ϕ	vegetation total solid volume fraction [—]
Ω	creek cross-sectional area [m^2]
ρ	seawater density [kg/m^3]

τ_{bed}	bed shear stress [N/m^2]
τ_{veg}	vegetation shear stress [N/m^2]

ORCID

Erik M. Horstman  <https://orcid.org/0000-0003-4261-1443>

Karin R. Bryan  <https://orcid.org/0000-0002-4480-740X>

Julia C. Mularney  <https://orcid.org/0000-0001-5190-3531>

REFERENCES

- Adame, M.F., Neil, D., Wright, S.F. & Lovelock, C.E. (2010) Sedimentation within and among mangrove forests along a gradient of geomorphological settings. *Estuarine, Coastal and Shelf Science*, 86(1), 21–30. <https://doi.org/10.1016/j.ecss.2009.10.013>
- Allen, J.R.L. (2000) Morphodynamics of Holocene salt marshes: a review sketch from the Atlantic and Southern North Sea coasts of Europe. *Quaternary Science Reviews*, 19(12), 1155–1231. [https://doi.org/10.1016/S0277-3791\(99\)00034-7](https://doi.org/10.1016/S0277-3791(99)00034-7)
- Alongi, D.M. (2009) *The energetics of mangrove forests*, 216 pp. Netherlands: Springer.
- Aucan, J. & Ridd, P.V. (2000) Tidal asymmetry in creeks surrounded by saltflats and mangroves with small swamp slopes. *Wetlands Ecol. Manage*, 8(4), 223–232. <https://doi.org/10.1023/a:1008459814925>
- Baptist, M.J., Babovic, V., Rodríguez Uthurburu, J., Keijzer, M., Uittenbogaard, R.E., Mynett, A. & Verwey, A. (2007) On inducing equations for vegetation resistance. *Journal of Hydraulic Research*, 45(4), 435–450. <https://doi.org/10.1080/00221686.2007.9521778>
- Bayliss-Smith, T.P., Healey, R., Lailey, R., Spencer, T. & Stoddart, D.R. (1979) Tidal flows in salt marsh creeks. *Estuarine and Coastal Marine Science*, 9(3), 235–255. [https://doi.org/10.1016/0302-3524\(79\)90038-0](https://doi.org/10.1016/0302-3524(79)90038-0)
- Bryan, K.R., Nardin, W., Mularney, J.C. & Fagherazzi, S. (2017) The role of cross-shore tidal dynamics in controlling intertidal sediment exchange in mangroves in Cù Lao Dung, Vietnam. *Continental Shelf Research*, 147(Supplement C), 128–143. <https://doi.org/10.1016/j.csr.2017.06.014>
- Christiansen, T., Wiberg, P.L. & Milligan, T.G. (2000) Flow and sediment transport on a tidal salt marsh surface. *Estuarine, Coastal and Shelf Science*, 50(3), 315–331. <https://doi.org/10.1006/ecss.2000.0548>
- D'Alpaos, A., Lanzoni, S., Marani, M. & Rinaldo, A. (2010) On the tidal prism–channel area relations. *Journal of Geophysical Research: Earth Surface*, 115, F01003. <https://doi.org/10.1029/2008jf001243>
- Duke, N.C., Ball, M.C. & Ellison, J.C. (1998) Factors influencing biodiversity and distributional gradients in mangroves. *Global Ecology & Biogeography Letters*, 7(1), 27–47. <https://doi.org/10.2307/2997695>
- Fagherazzi, S., Wiberg, P.L., Temmerman, S., Struyf, E., Zhao, Y. & Raymond, P. (2013) Fluxes of water, sediments, and biogeochemical compounds in salt marshes. *Ecological Processes*, 2(1), 3. <https://doi.org/10.1186/2192-1709-2-3>
- Friedrichs, C.T. (2010) Barotropic tides in channelized estuaries. In: Valle-Levinson, A. (Ed.) *Contemporary Issues in Estuarine Physics*. Cambridge, UK: Cambridge University Press, pp. 27–61.
- Friedrichs, C.T. & Aubrey, D.G. (1988) Non-linear tidal distortion in shallow well-mixed estuaries: a synthesis. *Estuarine, Coastal and Shelf Science*, 27(5), 521–545. [https://doi.org/10.1016/0272-7714\(88\)90082-0](https://doi.org/10.1016/0272-7714(88)90082-0)
- Friedrichs, C.T. & Aubrey, D.G. (1994) Tidal propagation in strongly convergent channels. *Journal of Geophysical Research: Oceans*, 99(C2), 3321–3336. <https://doi.org/10.1029/93JC03219>
- Friedrichs, C.T. & Madsen, O.S. (1992) Nonlinear diffusion of the tidal signal in frictionally dominated embayments. *Journal of Geophysical Research: Oceans*, 97(C4), 5637–5650. <https://doi.org/10.1029/92jc00354>
- Graeme, M. (2009) *Estuarine Vegetation Survey: Whitianga Harbour, Technical Report 2009/15*, 82 pp. Hamilton, New Zealand: Environment Waikato.
- Horstman, E.M., Bryan, K.R., Mularney, J.C., Pilditch, C.A. & Eager, C.A. (2018a) Are flow-vegetation interactions well represented by mimics? A case study of mangrove pneumatophores. *Advances in*

- Water Resources, 111, 360–371. <https://doi.org/10.1016/j.advwatres.2017.11.018>
- Horstman, E.M., Dohmen-Janssen, C.M., Bouma, T.J. & Hulscher, S.J.M.H. (2015) Tidal-scale flow routing and sedimentation in mangrove forests: combining field data and numerical modelling. *Geomorphology*, 228, 244–262. <https://doi.org/10.1016/j.geomorph.2014.08.011>
- Horstman, E.M., Dohmen-Janssen, C.M. & Hulscher, S.J.M.H. (2013) Flow routing in mangrove forests: a field study in Trang province, Thailand. *Continental Shelf Research*, 71, 52–67. <http://doi.org/10.1016/j.csr.2013.10.002>
- Horstman, E.M., Lundquist, C.J., Bryan, K.R., Bulmer, R.H., Mullarney, J.C. & Stokes, D.J. (2018b) The dynamics of expanding mangroves in New Zealand. In: Makowski, C. & Finkl, C.W. (Eds.) *Threats to Mangrove Forests: Hazards, Vulnerability, and Management*. Coastal Research Library. Vol. 25. Cham, Switzerland: Springer International Publishing AG, pp. 23–51. https://doi.org/10.1007/978-3-319-73016-5_2
- Jones, C.G., Lawton, J.H. & Shachak, M. (1994) Organisms as ecosystem engineers. *Oikos*, 69(3), 373–386. <https://doi.org/10.2307/3545850>
- Jones, C.G., Lawton, J.H. & Shachak, M. (1997) Positive and negative effects of organisms as physical ecosystem engineers. *Ecology*, 78(7), 1946–1957. [https://doi.org/10.1890/0012-9658\(1997\)078\[1946:PANEEO\]2.0.CO;2](https://doi.org/10.1890/0012-9658(1997)078[1946:PANEEO]2.0.CO;2)
- Jones, H. (2008) *Coastal Sedimentation: What We Know and the Information Gaps*. Environment Waikato Technical Report 2008/12. Hamilton, New Zealand: Waikato Regional Council.
- Krauss, K.W., Doyle, T.W., Doyle, T.J., Swarzenski, C.M., From, A.S., Day, R.H. & Conner, W.H. (2009) Water level observations in mangrove swamps during two hurricanes in Florida. *Wetlands*, 29(1), 142–149. <https://doi.org/10.1672/07-232.1>
- Lara, R.J., Szlafsztein, C.F., Cohen, M.C.L., Oxmann, J., Schmitt, B.B. & Filho, P.W.M.S. (2009) Geomorphology and sedimentology of mangroves and salt marshes: the formation of Geobotanical Units. In: Perillo, G.M.E., Wolanski, E., Cahoon, D.R. & Brinson, M.M. (Eds.) *Coastal wetlands: an integrated ecosystem approach*. Amsterdam: Elsevier, pp. 593–613.
- Larsen, L.G. (2019) Multiscale flow-vegetation-sediment feedbacks in low-gradient landscapes. *Geomorphology*, 334, 165–193. <https://doi.org/10.1016/j.geomorph.2019.03.009>
- Maza, M., Lara, J.L. & Losada, I.J. (2019) Experimental analysis of wave attenuation and drag forces in a realistic fringe Rhizophora mangrove forest. *Advances in Water Resources*, 131, 103376. <https://doi.org/10.1016/j.advwatres.2019.07.006>
- Mazda, Y., Kanazawa, N. & Wolanski, E. (1995) Tidal asymmetry in mangrove creeks. *Hydrobiologia*, 295(1), 51–58. <https://doi.org/10.1007/bf00029110>
- Mazda, Y., Kobashi, D. & Okada, S. (2005) Tidal-scale hydrodynamics within mangrove swamps. *Wetlands Ecology and Management*, 13(6), 647–655. <https://doi.org/10.1007/s11273-005-0613-4>
- McIvor, A.L., Spencer, T., Möller, I. & Spalding, M. (2012) *Storm surge reduction by mangroves*, 36 pp. Cambridge: Cambridge Coastal Research Unit.
- McIvor, A.L., Spencer, T., Möller, I. & Spalding, M. (2013) *The response of mangrove soil surface elevation to sea level rise*, 59 pp. Cambridge: Cambridge Coastal Research Unit.
- Montgomery, D.R. & Dietrich, W.E. (1992) Channel initiation and the problem of landscape scale. *Science*, 255(5046), 826–830. <https://doi.org/10.1126/science.255.5046.826>
- Montgomery, J.M., Bryan, K.R., Horstman, E.M. & Mullarney, J.C. (2018) Attenuation of tides and surges by mangroves: contrasting case studies from New Zealand. *Water*, 10(9), 1119. <https://doi.org/10.3390/w10091119>
- Montgomery, J.M., Bryan, K.R., Mullarney, J.C. & Horstman, E.M. (2019) Attenuation of storm surges by coastal mangroves. *Geophysical Research Letters*, 46(5), 2680–2689. <https://doi.org/10.1029/2018gl081636>
- Mullarney, J.C. & Henderson, S.M. (2018) Flows within marine vegetation canopies. In: Panchang, V. & Kaihatu, J. (Eds.) *Advances in Coastal Hydraulics*. Singapore: World Scientific Publishing Ltd., pp. 1–46. https://doi.org/10.1142/9789813231283_0001
- Mullarney, J.C., Henderson, S.M., Norris, B.K., Bryan, K.R., Fricke, A.T. & Sandwell, D.R. (2017a) A question of scale: the role of turbulence within mangrove roots in shaping the Mekong Delta. *Oceanography*, 30(3), 34–47. <http://doi.org/10.5670/oceanog.2017.312>
- Mullarney, J.C., Henderson, S.M., Reynolds, J.A.H., Norris, B.K. & Bryan, K.R. (2017b) Spatially varying drag within a wave-exposed mangrove forest and on the adjacent tidal flat. *Continental Shelf Research*, 147 (Supplement C), 102–113.
- Nepf, H.M. (1999) Drag, turbulence, and diffusion in flow through emergent vegetation. *Water Resources Research*, 35(2), 479–489. <http://doi.org/10.1029/1998wr900069>
- Nepf, H.M. (2012) Flow and transport in regions with aquatic vegetation. *Annual Review of Fluid Mechanics*, 44(1), 123–142. <http://doi.org/10.1146/annurev-fluid-120710-101048>
- Nortek AS. (2017) *The Comprehensive Manual*, 152 pp. Rud, Norway: Nortek AS.
- Perillo, G.M.E. (2019) Geomorphology of tidal courses and depressions. In: Perillo, G.M.E., Wolanski, E., Cahoon, D.R. & Hopkinson, C.S. (Eds.) *Coastal wetlands: an integrated ecosystem approach*. 2nd edition. Amsterdam: Elsevier, pp. 221–261. <https://doi.org/10.1016/B978-0-444-63893-9.00006-X>
- Pethick, J.S. (1980) Velocity surges and asymmetry in tidal channels. *Estuarine and Coastal Marine Science*, 11(3), 331–345. [https://doi.org/10.1016/S0302-3524\(80\)80087-9](https://doi.org/10.1016/S0302-3524(80)80087-9)
- Reeve, G.M.D. (2008) *Sedimentation and hydrodynamics of Whitianga estuary*. Hamilton, New Zealand: University of Waikato.
- Rinaldo, A., Fagherazzi, S., Lanzoni, S., Marani, M. & Dietrich, W.E. (1999a) Tidal networks: 2. Watershed delineation and comparative network morphology. *Water Resources Research*, 35(12), 3905–3917. <https://doi.org/10.1029/1999WR900237>
- Rinaldo, A., Fagherazzi, S., Lanzoni, S., Marani, M. & Dietrich, W.E. (1999b) Tidal networks: 3. Landscape-forming discharges and studies in empirical geomorphic relationships. *Water Resources Research*, 35(12), 3919–3929. <https://doi.org/10.1029/1999WR900238>
- Rusello, P.J., Lohrmann, A., Siegel, E. & Maddux, T. (2006) *Improvements in acoustic doppler velocimetry, paper presented at The 7th Int. ICHE*. Philadelphia, USA: Conf. on Hydroscience and Engineering.
- SonTek. (2000) *Triton Software Manual*, 46 pp. San Diego, USA: SonTek.
- Spalding, M., Kainuma, M. & Collins, L. (2010) *World Atlas of Mangroves*, 319 pp. London, UK: Earthscan.
- Speer, P.E., Aubrey, D.G. & Friedrichs, C.T. (1991) Nonlinear hydrodynamics of shallow tidal inlet/bay systems. In: Parker, B.B. (Ed.) *Tidal hydrodynamics*. New York: John Wiley, pp. 321–339.
- Stark, J., Van Oyen, T., Meire, P. & Temmerman, S. (2015) Observations of tidal and storm surge attenuation in a large tidal marsh. *Limnology and Oceanography*, 60(4), 1371–1381. <https://doi.org/10.1002/limo.10104>
- Temmerman, S., Bouma, T.J., Govers, G., Wang, Z.B., De Vries, M.B. & Herman, P.M.J. (2005) Impact of vegetation on flow routing and sedimentation patterns: three-dimensional modeling for a tidal marsh. *Journal of Geophysical Research*, 110(F4), F04019. <https://doi.org/10.1029/2005JF000301>
- Tinoco, R.O. & Coco, G. (2016) A laboratory study on sediment resuspension within arrays of rigid cylinders. *Advances in Water Resources*, 92, 1–9. <https://doi.org/10.1016/j.advwatres.2016.04.003>
- Tinoco, R.O. & Cowen, E.A. (2013) The direct and indirect measurement of boundary stress and drag on individual and complex arrays of elements. *Experiments in Fluids*, 54(4), 1509. <https://doi.org/10.1007/s00348-013-1509-3>
- Tinoco, R.O., San Juan, J.E. & Mullarney, J.C. (2020) Simplification bias: lessons from laboratory and field experiments on flow through aquatic vegetation. *Earth Surface Processes and Landforms*, 45(1), 121–143. <https://doi.org/10.1002/espl.4743>
- Tomlinson, P.B. (1986) *The botany of mangroves*, 423 pp. Cambridge, UK: Cambridge University Press.
- Twilley, R.R. & Rivera-Monroy, V.H. (2009) Ecogeomorphic models of nutrient biogeochemistry for mangrove wetlands. In: Perillo, G.M.E., Wolanski, E., Cahoon, D.R. & Brinson, M.M. (Eds.) *Coastal wetlands: an integrated ecosystem approach*. Amsterdam: Elsevier, pp. 641–683.

- Twilley, R.R., Rivera-Monroy, V.H., Chen, R. & Botero, L. (1999) Adapting an ecological mangrove model to simulate trajectories in restoration ecology. *Marine Pollution Bulletin*, 37(8–12), 404–419. [https://doi.org/10.1016/S0025-326X\(99\)00137-X](https://doi.org/10.1016/S0025-326X(99)00137-X)
- Van Loon, A.F., Dijksma, R. & Van Mensvoort, M.E.F. (2007) Hydrological classification in mangrove areas: a case study in Can Gio. *Aquatic Botany*, 87(1), 80–82. <https://doi.org/10.1016/j.aquabot.2007.02.001>
- Van Santen, P., Augustinus, P.G.E.F., Janssen-Stelder, B.M., Quartel, S. & Tri, N.H. (2007) Sedimentation in an estuarine mangrove system. *Journal of Asian Earth Sciences*, 29(4), 566–575. <https://doi.org/10.1016/j.jseaes.2006.05.011>
- Vandenbruwaene, W., Schwarz, C., Bouma, T.J., Meire, P. & Temmerman, S. (2015) Landscape-scale flow patterns over a vegetated tidal marsh and an unvegetated tidal flat: implications for the landform properties of the intertidal floodplain. *Geomorphology*, 231, 40–52. <https://doi.org/10.1016/j.geomorph.2014.11.020>
- Wamsley, T.V., Cialone, M.A., Smith, J.M., Atkinson, J.H. & Rosati, J.D. (2010) The potential of wetlands in reducing storm surge. *Ocean Engineering*, 37(1), 59–68. <https://doi.org/10.1016/j.oceaneng.2009.07.018>
- Watson, J.G. (1928) *Mangrove forests of the Malay Peninsula*, 275 pp. Kuala Lumpur: Federated Malay States Government.
- Willemse, P.W.J.M., Horstman, E.M., Borsje, B.W., Friess, D.A. & Dohmen-Janssen, C.M. (2016) Sensitivity of the sediment trapping capacity of an estuarine mangrove forest. *Geomorphology*, 273, 189–201. <https://doi.org/10.1016/j.geomorph.2016.07.038>
- Wolanski, E. (1992) Hydrodynamics of mangrove swamps and their coastal waters. *Hydrobiologia*, 247(1–3), 141–161. <https://doi.org/10.1007/BF00008214>
- Wolanski, E. (1995) Transport of sediment in mangrove swamps. *Hydrobiologia*, 295(1–3), 31–42. <https://doi.org/10.1007/BF00029108>
- Wolanski, E., Jones, M. & Bunt, J.S. (1980) Hydrodynamics of a tidal creek-mangrove swamp system. *Marine and Freshwater Research*, 31(4), 431–450. <https://doi.org/10.1071/MF9800431>
- Young, D.L., Bruder, B.L., Haas, K.A. & Webster, D.R. (2016) The hydrodynamics of surface tidal flow exchange in saltmarshes. *Estuarine, Coastal and Shelf Science*, 172, 128–137. <https://doi.org/10.1016/j.ecss.2016.02.006>
- Zhang, K., Liu, H., Li, Y., Xu, H., Shen, J., Rhome, J. & Smith III, T.J. (2012) The role of mangroves in attenuating storm surges. *Estuarine, Coastal and Shelf Science*, 102–103, 11–23.

SUPPORTING INFORMATION

Additional supporting information may be found online in the Supporting Information section at the end of this article.

How to cite this article: Horstman EM, Bryan KR, Mullarney JC. Drag variations, tidal asymmetry and tidal range changes in a mangrove creek system. *Earth Surf. Process. Landforms*. 2021;46:1828–1846. <https://doi.org/10.1002/esp.5124>